

RESEARCH ARTICLE

10.1002/2017JB014499

Key Points:

- We estimate the uplift rate of the Western Transverse Ranges in southern California from integrated GPS, InSAR, leveling, and tide gauge data
- Geodetic imaging of topographic growth reveals the vertical response to contraction across the Big Bend of the San Andreas Fault system
- Geographically continuous uplift of 1–2 mm/yr is asymmetric across the San Andreas Fault and decreases to subsidence near the coast

Supporting Information:

- Supporting Information S1

Correspondence to:

W. C. Hammond,
whammond@unr.edu

Citation:

Hammond, W. C., Burgette, R. J., Johnson, K. M., & Blewitt, G. (2018). Uplift of the Western Transverse Ranges and Ventura area of Southern California: A four-technique geodetic study combining GPS, InSAR, leveling, and tide gauges. *Journal of Geophysical Research: Solid Earth*, 123, 836–858. <https://doi.org/10.1002/2017JB014499>




Received 31 MAY 2017

Accepted 21 DEC 2017

Accepted article online 28 DEC 2017

Published online 15 JAN 2018

Uplift of the Western Transverse Ranges and Ventura Area of Southern California: A Four-Technique Geodetic Study Combining GPS, InSAR, Leveling, and Tide Gauges

William C. Hammond¹ , Reed J. Burgette², Kaj M. Johnson³ , and Geoffrey Blewitt¹ 
¹Nevada Geodetic Laboratory, Nevada Bureau of Mines and Geology, University of Nevada, Reno, NV, USA, ²Department of Geological Sciences, New Mexico State University, Las Cruces, NM, USA, ³Department of Geological Sciences, Indiana University, Bloomington, IN, USA

Abstract We estimate the rate of vertical land motion (VLM) in the region around the Western Transverse Ranges (WTR), Ventura, and Big Bend of the San Andreas Fault (SAF) of southern California using data from four geodetic techniques: GPS, interferometric synthetic aperture radar (InSAR), leveling, and tide gauges. We use a new analysis technique called GPS Imaging to combine the techniques and leverage the synergy between (1) high geographic resolution of InSAR, (2) precision, stability, and geocentric reference frame of GPS, (3) decades long observation of VLM with respect to the sea surface from tide gauges, and (4) relative VLM along dense leveling lines. The uncertainty in the overall rate field is ~1 mm/yr, though some individual techniques have uncertainties as small as 0.2 mm/yr. The most rapid signals are attributable to subsidence in aquifers and groundwater changes. Uplift of the WTR is geographically continuous, adjacent to the SAF and appears related to active crustal contraction across Pacific/North America plate boundary fault system. Uplift of the WTR and San Gabriel Mountains is ~2 mm/yr and is asymmetrically focused west of the SAF, consistent with interseismic strain accumulation across thrust faults in the Ventura area and Santa Barbara channel that accommodate contraction against the near vertical SAF.

Plain Language Summary How fast do mountains grow? What mechanism is forcing their growth? In our study we combined large and complementary data sets collected over the past century to estimate the current rate of mountain growth and land subsidence in the Ventura area and Western Transverse Ranges of southern California. We show that the rock of the mountains moves upward ~2 mm/yr across a large region between the San Andreas Fault and the Pacific coast. This rate seems slow on human terms but cumulatively amounts to 2 km of elevation per million years, which is a lot of topography that can be developed over geologic time, though it will be partially offset by the cumulative effects of erosion over similar amounts of time. Additional to the rapid mountain growth rate, these results are interesting because they place new constraints on the seismic potential of the active thrust faults that build the Western Transverse Ranges through plate tectonic forces. These new constraints help locate and estimate the pace at which active faults slip, thereby improving estimates of earthquake and tsunami hazards.

1. Introduction

The Western Transverse Ranges (WTR) have some of the highest contemporary crustal contraction and uplift rates in the cordillera of the western United States. Strain in the crust is seen in the topography of the ranges, uplift and deformation of marine terraces (McCrary and Lajoie, 1979; Rockwell et al., 1988; Yerkes & Lee, 1979, 1987; Yerkes et al., 1987), active contraction and shear from GPS geodesy (e.g., Donnellan et al., 1993; Marshall et al., 2013; Meade & Hager, 2005; McCaffrey, 2005), paleomagnetic rotations (Luyendyk et al., 1985), and thrust earthquake focal mechanisms (Jackson & Molnar, 1990). Over the time scale of 10⁴ to 10⁶ years, coastal uplift rates are generally 1 mm/yr or less (see, e.g., the SCEC vertical motion database, Niemi et al., 2008). However, along the system of thrust faults that forms the structural southern boundary of the WTR, they are significantly higher. For example, the Ventura Anticline uplift has been near 4–7 mm/yr (Hubbard et al., 2014; Niemi et al., 2008; Rockwell et al., 2016) and may indicate that the bounding thrust faults have the capacity to generate large earthquakes, up to *M* 8 (Dolan & Rockwell, 2001; McAuliffe et al., 2015).

Here we show that geodesy can directly measure the active uplift and subsidence across the WTR in order to provide improved constraints on vertical land motion (VLM) and argue that much of the signal is attributable to active tectonic deformation. VLM can result from multiple physical mechanisms, some of which, such as

the seasonal to intradecadal changes in hydrological effects (e.g., Amos et al., 2014; Argus et al., 2005; Bawden et al., 2001; Borsa et al., 2014), are transient in nature. Resolving the long-term trends and separating them from transient movement provides needed complementary information to resolve the pattern of tectonic strain accumulation across the plate boundary. There have been many studies of the horizontal interseismic motion across the Pacific/North America plate boundary zone in southern California (e.g., compilation by Sandwell et al., 2016), but direct geodetic observation of VLM remains difficult, and a consensus over the pattern and rates has not yet formed, with recent studies finding somewhat different signals and interpretation of their significance (e.g., Dong et al., 2006; Fay et al., 2008; Howell et al., 2016; Marshall et al., 2013, 2017; Tape et al., 2009). Interpreting interseismic VLM with slip rates on specific fault systems requires detailed modeling that accounts for the relationship between interseismic and long-term vertical deformation (e.g., Huang et al., 2010). We here concentrate on developing the most precise and detailed map of geodetic VLM to date so that improved models that better localize and quantify loading rate of faults can be developed in subsequent studies. Models of VLM are also needed for other purposes such as sea level studies which correct tide gauge records for VLM (Hamlington et al., 2016; Wöppelmann & Marcos, 2016) and similarly require separation of transient motions from long-term trends.

In the past VLM attributable to tectonic deformation has been difficult to detect owing to several factors. In GPS, for example, the accuracy and precision is poorer in the vertical coordinate owing to dilution of precision (Hofmann-Wellenhof et al., 1992), reliance on models of atmospheric refraction using globally representative approximations (Boehm et al., 2006), and contributions to vertical position from atmospheric pressure (Tregoning & Watson, 2009; van Dam et al., 1994) and hydrological loading (e.g., Borsa et al., 2014; Wahr et al., 2013). Interferometric synthetic aperture radar (InSAR) data complement GPS, providing blanket coverage, but suffer from errors in long-wavelength deformation owing to uncertainties in orbits, refractivity of the troposphere, topographic effects, and difficulties in unwrapping of phase (Chen & Zebker, 2000; Bürgmann et al., 2000; Massonnet & Feigl, 1998). Furthermore, InSAR is sensitive to Earth surface motion only along the satellite to ground line of sight direction, leaving the three-component direction of motion ambiguous. Conversely, tide gauge records are sensitive to VLM and have stable records, in some cases nearly a century long, but they use as a reference the mean surface of the ocean and hence are impacted by uncertainties in global mean sea level rise and oceanographic changes (e.g., Burgette et al., 2009; Wöppelmann & Marcos, 2016). Terrestrial leveling data also constrain VLM along dense lines usually surveyed along highways but suffer from atmospheric refraction and monument noise (Stein et al., 1986; Strange, 1981).

To overcome some of these challenges we here take advantage of improvements in the quality, quantity, and scope of data, and new analysis tools that improve the robustness of trend and field estimation from the data. We combine data from each of the four geodetic systems mentioned above (Figure 1) to develop an integrated field of VLM in a GPS-defined reference frame. A centerpiece to the improved analysis strategy is the use of the MIDAS and GPS Imaging algorithms that apply robust temporal and spatial filtering to stabilize the alignments so that they become insensitive to common problems in the data that can be exacerbated through least squares analysis (Blewitt et al., 2016; Hammond et al., 2016). The greater robustness, detail, and scope of the solution, along with solutions for the amplitude of seasonal motion, allow us to estimate which of the observed signals are attributable to tectonic motion and which to other processes.

2. Data

2.1. Global Positioning System (GPS)

California has some of the most dense and extensive GPS networks in the world. We use data from the regional high-precision GPS networks including the EarthScope Plate Boundary Observatory (PBO, operated by UNAVCO), Bay Area Regional Deformation Network (BARD, operated by UC Berkeley and the USGS), Continuously Operating Reference Station (CORS, coordinated by the National Geodetic Survey), and other stations in the network formerly known as SCIGN that are now operated by the USGS in Pasadena, Scripps Orbit and Permanent Array Center (SOPAC), and the Jet Propulsion Laboratory (JPL). Because we are primarily concerned with data that can provide constraint on vertical motions, we use relatively stringent criteria for accepting stations as data sources. We use stations that have over 5 years of data between their first and last occupation, have time series over 25% complete between the first and last observation, and have vertical rate

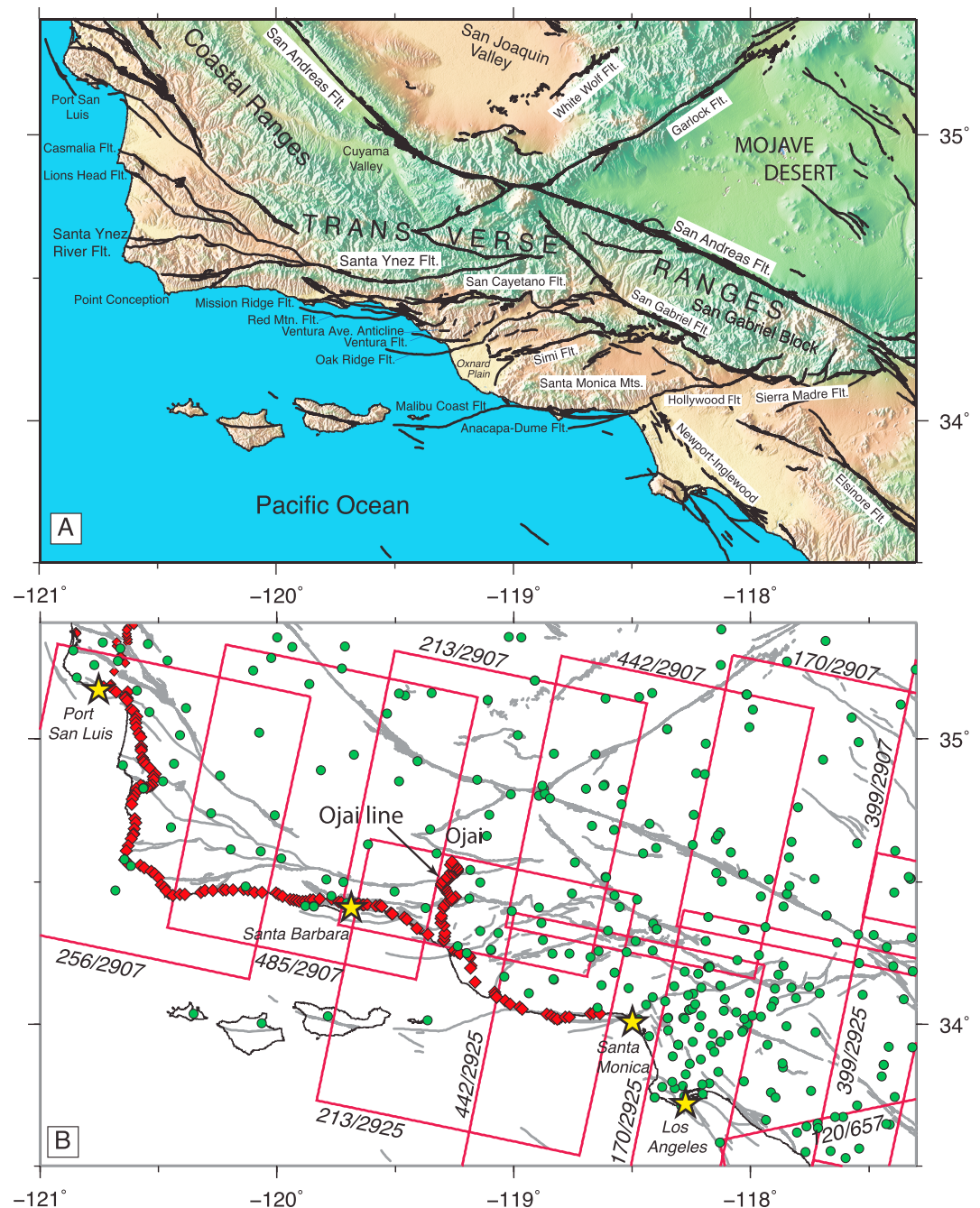


Figure 1. (a) Study area showing the topography and active crustal faults in southern California and WTR. VAA = Ventura Avenue anticline. (b) Locations of four geodetic techniques used in the study. InSAR track/frame sets are shown with red polygons annotated to show track/frame identification. Tide gauge locations are shown with yellow stars. Leveling lines are shown with small red diamonds. Location of GPS stations are shown with green dots.

uncertainties estimated from the time series of less than 1 mm/yr. We use all data available up until 26 January 2017. Within the area of Figure 1, 236 stations meet our criteria, 19 of which are designated IGS Core stations (<http://www.igs.org/network>).

We process RINEX data from the GPS stations to estimate daily coordinate time series as part of a global GPS network analysis that includes data from over 16,300 stations. We use the GIPSY-OASIS II software package in precise positioning mode (Zumberge et al., 1997) to estimate daily station coordinates. The processing uses reanalyzed fiducial-free GPS satellite orbit and clock parameters provided by the Jet

Propulsion Laboratory's IGS Analysis Center with antenna calibration models for station receivers and satellite transmitters. The observation model includes solid earth tides and oceanic tidal loading (Scherneck, 1991). The Global Mapping Function was applied to model tropospheric refractivity (Boehm et al., 2006), and the tropospheric wet delay was modeled as a random walk zenith parameter with two random walk horizontal gradient parameters (Bar Sever et al., 1998). The carrier phase ambiguities are resolved using the WLPB method (Bertiger et al., 2010).

We align the daily three-component position solutions with a custom North America-fixed, spatially filtered reference frame, NA12 (Blewitt et al., 2013). This frame has an origin and scale that are consistent with the International Terrestrial Reference Frame, ITRF2008 (Altamimi et al., 2011), but corotates with the North American plate and provides a continental scale regional filtering that reduces common-mode noise in the horizontal and vertical coordinates (Wdowski et al., 1997). The seven-parameter daily coordinate transformations from the JPL fiducial-free frame to NA12 are publicly available for GIPSY-OASIS II users at <ftp://gnss.nbm.unr.edu/x-files>. All position solutions are posted and available for download on the data products pages of the Nevada Geodetic Laboratory (<http://geodesy.unr.edu>).

We estimate vertical rates from GPS data using the MIDAS algorithm (Blewitt et al., 2016). This method incorporates a median-based nonparametric estimation of the trend that is highly insensitive to the presence of steps, outliers, and seasonal oscillations in the coordinate time series. MIDAS finds the mode of a distribution of rates using selected pairs of epochs separated by about 1 year, following median trend estimator theory (Sen, 1968; Theil, 1950). Since the pairs are about 1 year apart, the rates are insensitive to seasonality regardless of the details of its form (e.g., sinusoidal, sawtooth). Information about known steps owing to, for example, equipment changes or earthquakes is not critical, because the method is also insensitive to the presence of steps. Nonetheless we incorporate information from station metadata to more optimally select position pairs representative of the trend. MIDAS is the most accurate estimation method among those subjected to blind tests on synthetic data (Gazeaux et al., 2013). Uncertainties in the rates are estimated from the spread of the distribution of rate samples. Up to date MIDAS rates and uncertainties are generated weekly and are openly available for all stations processed by the Nevada Geodetic Laboratory at <http://geodesy.unr.edu>. Their values as of 26 January 2017, used in this analysis, are given in Table S1 in the supporting information. The median MIDAS rate uncertainty for stations in Figure 1 is 0.51 mm/yr, and all are less than 1.0 mm/yr owing to the exclusion criteria (Figure 2c). MIDAS uncertainties are a function of the amount of scatter the data have around the best trend and are usually larger than the formal uncertainties estimated in least squares inversions.

The distribution of vertical rates has a median value near zero, (0.05 mm/yr) showing that the region does not experience significant net uplift or subsidence with respect to the NA12 reference frame origin (Figure 2a). The distribution of vertical rates is asymmetric, with a long tail toward negative values of vertical rate (subsidence). This skewness is attributable to GPS stations that are located on active aquifers or groundwater basins in southern California that have moved generally more downward, at speeds greater than tectonic vertical rates, since observation began. These GPS stations are usually dominated by nontectonic signals. In Figure 3 we show a map of GPS vertical velocity obtained using our GPS Imaging algorithm (Hammond et al., 2016) on the vertical MIDAS velocities. This map serves as a starting point and reference for the combinations and already shows some intriguing zones of uplift and subsidence that we will discuss in further detail below.

2.2. InSAR

We use radar scenes collected by the C-band ERS-1, ERS-2, and ENVISAT satellites operated by the European Space Agency between 1992 and 2009, which we obtained from the WinSAR archive at UNAVCO. We used all the radar scenes from a given mission/track/frame set if there were 16 or greater number of scenes available from which we were able to perform interferometry using the Gamma software. From the raw data we were able to generate between 16 and 153 single-look complex (SLC) images for each set with common mission, track, and frame number. Most of the data were from descending orbits because they tend to have a greater number of scenes available per mission/track/frame set. However, we were able to make 28 SLC images from track 120 frame 657, so we used this set to provide additional constraint on vertical motions in the southeast corner of our study area (Figure 1b). Table 1 summarizes the track/frame sets used, the number of SLCs obtained, the number of interferograms that were obtained, and range of dates covered by the data. Baseline plots showing all interferometric pairs are provided in the supporting information. For

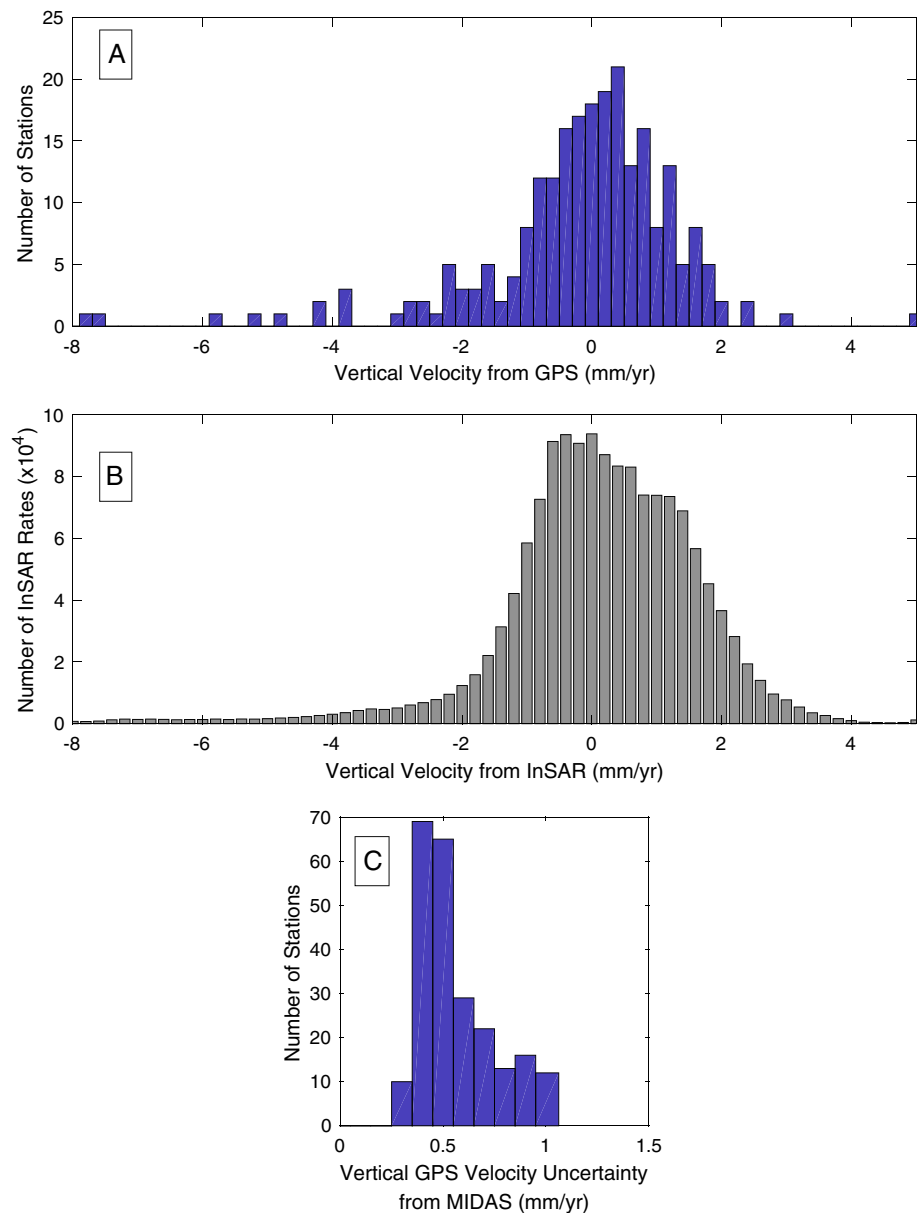


Figure 2. Histograms of (a) vertical GPS velocity, (b) InSAR-based vertical velocity after projecting to vertical and alignment with other techniques, and (c) uncertainty in the vertical GPS rate from the MIDAS algorithm.

coregistration of images we selected a reference scene for each mission/track/frame set. The reference scene was the one with median latitude among those with an area within 10% of the median scene area, where area and central latitude are calculated from the convex hull of the locations with nonempty phase rate values. In some cases we obtained scenes that could have been matched with adjacent scenes along track and concatenated to make longer single scenes, which can be advantageous for eliminating discontinuities between InSAR rate maps that are adjacent in the along-track direction. We did not, however, perform this concatenation, instead choosing to keep scenes in their original dimensions. There were several reasons for this including (1) owing to availability of scenes in the WinSAR archive different numbers of scenes were available in adjacent along-track frames, so using only scenes combined along track would require omitting some data when we were seeking to use the maximum amount possible, (2) combining scenes along track only addresses along-track seams, and not cross-track seams so the net benefit of combining along-track scenes is limited. Later in the analysis (section 3.1.6) we discuss the resulting seams and how their magnitudes are small compared to the overall error budget in VLM.

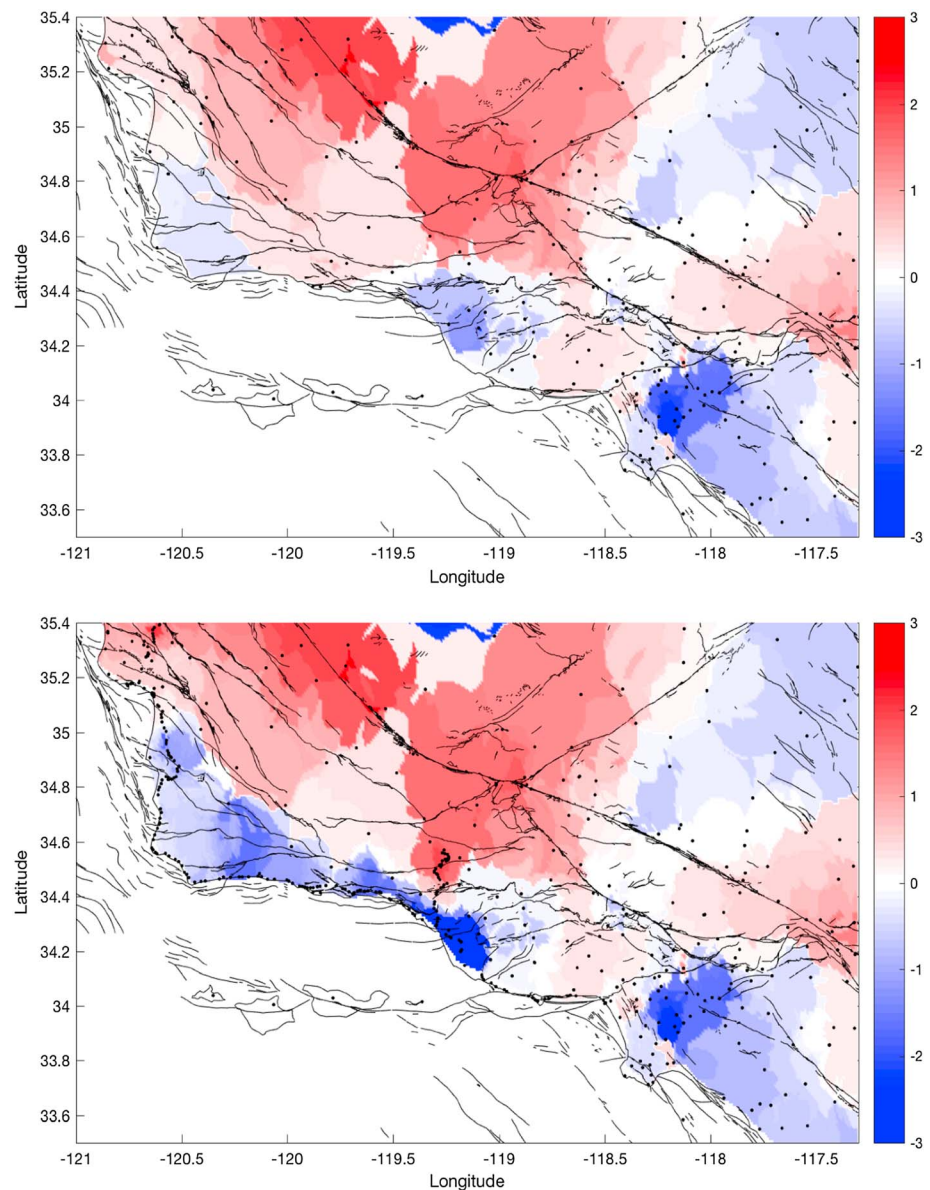


Figure 3. (top) GPS Imaging of vertical MIDAS rates using method of Hammond et al. (2016). Color scale is in mm/yr, dots are locations of GPS stations used in the analysis, black lines are active faults. (bottom) Same image but constructed using both GPS, tide gauge, and leveling data that have been aligned together in the same reference frame. Color scale bar in mm/yr.

We performed two-pass interferometry on all pairs of scenes that had a perpendicular baseline less than 300 m with a DEM generated from SRTM data for the area covered in Figure 1. For each group of scenes in a given mission/track/frame set, the needed DEM tiles were downloaded from the USGS and combined into a single file covering the area of the radar scenes. For each pair we applied adaptive spectral filtering (Goldstein & Werner, 1998) and median cost flow unwrapping of the phase (Costantini, 1998) and solved for corrections to the baselines using the relationship between topography and phase, as implemented in the Gamma software package (Werner et al., 2000). We exclude InSAR data for parts of scenes on the islands of San Miguel, Santa Rosa, and Santa Cruz across the Santa Barbara Channel. For each mission/track/frame set we solve for rates of motion in the satellite line of sight (LOS) direction at every pixel in the coregistered interferograms using the SBAS algorithm (Berardino et al., 2002). Before applying SBAS we exclude pixels that have a coherence value of less than 0.3 and exclude entire interferograms that have 25% or less of their area above this threshold. We also exclude interferograms with very high RMS phase or phase rate values in the

Table 1
InSAR Track/Frame Sets Used in Analysis

Platform	Track	Frame	Asc./ Desc.	Number RSLCs	Number interferograms	Date of first scene ^a	Date of last scene ^a
ENVISAT	120	657	A	28	142	20031029	20090624
ENVISAT	170	2907	D	22	104	20040807	20090627
ENVISAT	170	2925	D	36	306	20030927	20090627
ENVISAT	213	2907	D	18	89	20050201	20090526
ENVISAT	213	2925	D	16	57	20050201	20090526
ENVISAT	399	2907	D	34	287	20030908	20090608
ENVISAT	399	2925	D	35	300	20030630	20090608
ENVISAT	442	2907	D	22	101	20030424	20090611
ENVISAT	442	2925	D	25	144	20030424	20090611
ENVISAT	485	2907	D	54	540	20030112	20090823
ERS	170	2925	D	143	2,525	19920930	20091114
ERS	170	2907	D	129	2114	19920617	20091219
ERS	213	2907	D	122	182	19920516	20091222
ERS	213	2925	D	125	626	19920620	20091222
ERS	256	2907	D	67	578	19920414	20080822
ERS	399	2907	D	153	2590	19920424	20091130
ERS	399	2925	D	152	2367	19920424	20091130
ERS	442	2907	D	139	287	19920914	20091203
ERS	442	2925	D	148	449	19920914	20091203
ERS	485	2907	D	130	479	19920604	20091206

^aDate format is yyyyymmdd.

deramped interferograms since they contain unusually large errors. These criteria generally excluded less than 5% of the interferograms in a given track/frame set. In the SBAS inversion we include parameters for a constant velocity plus annual period sine and cosine terms. We filled gaps from locations with poor coherence and applied Gaussian smoothing with a wavelength of ~2 km to the LOS velocity map. In all we calculated 20 overlapping LOS rate images, which we used to construct a mosaic of vertical rate described below.

2.3. Tide Gauges

We use relative sea level (RSL) time series recorded by NOAA at tide gauges in Southern California to estimate relative rates of VLM over the past century. Tide gauges measure sea level changes over time relative to the crust to which they are attached, and thus are sensitive to signals from both oceanic and crustal processes. Repeated local leveling between tide gauge sensors and a network of nearby benchmarks maintains the local vertical control on the height of the tide gauges. As a result, the relative vertical deformation sensed by the tide gauge is specific to the primary benchmark at each tide gauge that defines the local datum. Over the regional spatial scale of the study area, estimated variations in the rate of geocentric sea level rise are <0.2 mm/yr (Church et al., 2004), and most of the ocean noise is shared between tide gauges. The Los Angeles, Santa Monica, and Port San Luis tide gauges bound our study area along the coast (Figure 1) and have nearly continuous records that span ≥70 year (Figure 4). The Santa Barbara tide gauge has a more discontinuous record that began in 1973.

We use monthly mean relative sea level time series from a network including other long-running tide gauges along the California coast from San Diego to San Francisco. In the processing of these data we difference the time series of pairs of tide gauges to remove shared oceanographic noise, which yields more precise estimates of relative vertical motion between gauges (Figure 4). We estimate the rates and uncertainties of relative sea level change from both the undifferenced time series from long-running (>70 year duration) tide gauges and the differenced time series of many pairs of tide gauges, taking into account time-correlated noise using the CATS algorithm (Williams, 2008). We apply the network solution method of Burgette et al. (2013) to estimate rates and uncertainties of relative sea level change at all gauges.

Adjusted RSL rates in the network solution have estimated precision of 0.2–0.4 mm/yr and show significant differences in the rate of relative sea level change over the ~100 km distances between tide gauges (Table 2). The observed rate of RSL rise in the Los Angeles and Western Transverse Ranges area is significantly lower

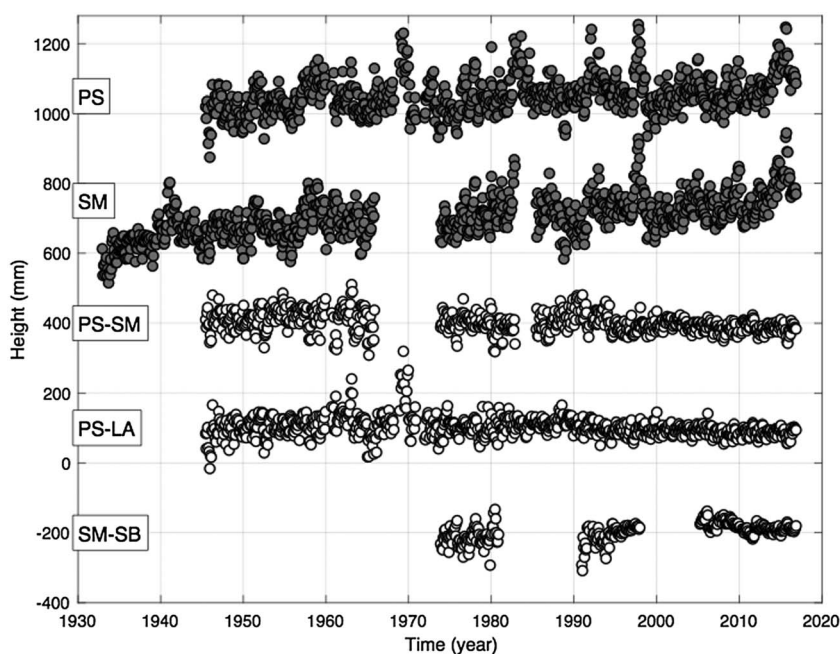


Figure 4. Example tide gauge records for Port San Luis (PS) and Santa Monica (SM) showing sea surface height with respect to land (gray circles). Lower three time series are example differenced tide gauge records between PS, SM, and the LA (Los Angeles) and SB (Santa Barbara) gauges (white circles). Time series vertical shift is arbitrary for presentation clarity.

than the ~ 2.0 mm/yr rates observed in the San Diego and San Francisco areas to the south and north, with the lowest rates observed at the Santa Barbara and Port San Luis tide gauges (Table 2). Assuming a published value for the geocentric sea level rates allows estimation of the geocentric rate of VLM at the tide gauges. However, the geocentric rate of sea level change is not well resolved at the sub-1 mm/yr level at the regional scale (e.g., Spada & Galassi, 2012), and the relative sea level rates are most useful to define the differential vertical rates between tide gauges.

2.4. Leveling

Leveling data provide spatially dense and precise estimates of vertical deformation spanning 30–70 years along two routes that cross the major structures associated with the Ventura Basin and WTR (Buchanan-Banks et al., 1975). We use the unadjusted line data, with orthometric, rod, level, temperature, astronomical, refraction, and magnetic corrections applied by the National Geodetic Survey as appropriate (Federal Geodetic Control Committee, 1984). We analyzed 23 first-order and 2 second-order leveling lines that repeatedly surveyed a coastal route between the Santa Monica and Port San Luis tide gauges and a route north through the ranges along Ventura Avenue, extending to Ojai along Highway 33 (Figure 1, Table 3).

Table 2

Tide Gauge Locations, Spans of Data, Estimated Rates and Uncertainties

Tide gauge	Longitude	Latitude	Start	End	Total months	Adjusted rate (mm/yr)	Adjusted rate uncertainty (mm/yr)
San Diego	−117.173	32.714	1906.04	2016.96	1,317	2.04	0.21
La Jolla	−117.258	32.867	1924.87	2016.96	1,071	2.04	0.23
Newport Beach	−117.883	33.603	1955.62	1993.96	461	1.89	0.33
Los Angeles	−118.272	33.720	1923.96	2016.96	1,117	0.87	0.22
Santa Monica	−118.499	34.008	1933.04	2016.96	879	1.25	0.28
Santa Barbara	−119.690	34.406	1973.96	2016.96	306	0.04	0.36
Port San Luis	−120.757	35.172	1945.54	2016.96	823	0.71	0.28
Monterey	−121.889	36.605	1973.96	2016.96	517	1.27	0.40
San Francisco	−122.465	37.807	1900.04	2016.96	1,402	1.91	0.29

Table 3
Leveling Lines Used in This Study

Line name	Order/class	Mean date	Precision (mm) ^a
74203	1/2	1920.055	21.58
82725	1/2	1928.719	1.73
L1766	1/2	1934.323	1.31
L5800	2/0	1935.242	1.84
L8470	1/2	1939.051	1.3
L8470	1/2	1939.051	1.3
L8687	1/2	1939.763	1.66
L9449	1/2	1942.092	1.34
L10511	2/0	1943.193	3.23
L12128	1/2	1947.419	2.68
L15972	1/2	1956.411	1.42
L15975	1/2	1956.336	1.39
L16345	1/2	1956.998	1.59
L17778	1/2	1960.152	1.77
L17847	1/2	1960.253	1.37
L17853	1/2	1960.342	1.24
L21366	1/1	1968.220	0.57
L23882	1/1	1974.556	0.75
L24298	1/1	1978.078	0.63
L24301/2	1/1	1978.179	0.69
L24301/1	1/1	1978.197	0.66
L24835	1/2	1983.433	1.43
L25174	1/2	1989.379	0.99
L25177	1/2	1989.441	1.16
L25180	1/2	1989.490	0.99

^aReported uncertainty over 1 km distance. For lines that were not double-run over the full line length, the reported precision is for single-run leveling.

We have developed a new analysis strategy that takes advantage of the large volume of available data and estimates relative uplift rates of benchmarks surveyed in multiple epochs with a time-series approach. First, we combine overlapping lines that were surveyed in the same year into longer continuous lines based on the elevations of benchmarks at the line junctions. Next, we select sections of the leveling routes covered by a consistent set of leveling lines observed in multiple epochs. We then shift the benchmark elevations in this set of line data to match on a common reference benchmark, selecting a stable one with the maximum number of epochs. This generates relative heights of each benchmark along the route relative to the reference mark at the observed epochs, and we analyze the time series of relative vertical displacements for each benchmark observed in at least three epochs. Based on preliminary inspection, we exclude two leveling lines surveyed in the period of 1968–1971 because the elevation data from these epochs are outliers in the time series for many benchmarks, which may indicate systematic error. Least squares lines fit to the benchmark elevation time series provide estimates of rates and uncertainties of vertical motion of benchmarks relative to the reference benchmark. The rate uncertainties from the misfit to the linear model encompass both local benchmark stability as well as survey errors.

The coastal leveling route between the Santa Monica and Port San Luis tide gauges comprises four sections of leveling data analyzed in this fashion, and the Ojai line and three smaller sections north of Port San Luis form spurs off of the main route. Rates from sections of the leveling network are shifted into alignment with neighboring sections at junctions where common benchmarks are included in two sections. This yields relative uplift rates across the full leveling network in a consistent, local reference frame defined by one of the section reference benchmarks. Notably, the leveling

rate field includes the primary benchmarks of tide gauges along the route. Thus, following the adjustments of the leveling data, the tide gauge rates (Table 2) and leveling rates (Table 3) are aligned and refer to the same datum.

Lastly, we exclude locally unstable benchmarks with discrepancies in vertical rate > 1 mm/yr relative to neighboring monuments as defined by a median calculated over a 10 km moving window in run distance. The threshold is increased to 2 mm/yr in areas of rapid subsidence, where the steep spatial gradients in uplift rate are not well characterized by the moving median. These thresholds greatly exceed the estimated 0.2 mm/yr 1 sigma uncertainty over 10 km estimated for random leveling error. Of the 226 total benchmarks, 25 were excluded as being locally unstable, with 22 of these subsiding relative to neighboring monuments. This tendency of $>85\%$ of unstable benchmarks settling is similar to previous observations from Cascadia (Burgette et al., 2009).

Uncertainties in the leveling-derived uplift rates due to accumulated random survey error are estimated using median precisions for the leveling lines involved as reported in the NGS data, and a common time span based on the median time span of observations for the benchmarks in the analysis (Burgette et al., 2009). These uncertainties grow with the square root of distance from the tide gauges and inland from the coast for the spur line north from Ventura. The rate uncertainties from the distance-dependent survey error are combined in quadrature with the estimated benchmark-specific uncertainties derived from the time series analysis to obtain the total rate uncertainty.

3. Analysis

3.1. Alignments and Mosaicking

To align all of the techniques together we create a mosaic of vertical rates by aligning each rate field with the GPS-defined reference frame. The alignment procedure occurs in four main steps: (1) Estimate and subtract geographically constant shifts between leveling/tide gauge and GPS vertical rates, (2) align each InSAR

mission/track/frame set to the GPS LOS rates, (3) remove the signal of known horizontal deformation from the InSAR LOS and project the remaining signal into the vertical direction, and (4) align each InSAR vertical rate map into a mosaic map of the estimated vertical rate field.

3.1.1. GPS Imaging

To estimate and remove differences in rates between the data sets, we use the GPS Imaging algorithm, which was originally developed to perform robust despeckling, filtering, and interpolation of vertical rate fields from GPS data (Hammond et al., 2016). The algorithm identifies the part of a spatially variable signal that is locally consistent among multiple stations, making it insensitive to outlying rates of arbitrary magnitude as long as they are isolated, that is, present locally in only a single station. First, filtering is applied to point data (e.g., at GPS stations) so that the value at every station is replaced by the weighted median of values at neighboring stations connected via a Delaunay triangulation of the network. Interpolation of the filtered field is achieved by introducing a grid, and at every point performing an ad hoc triangulation to the nearest GPS stations and assigning the weighted median of the nearest vertical rates to the grid point. In the resulting interpolation, the value at every point is a function only of the values at neighboring stations, so the geographic resolution of the derived field is a function only of the GPS network spacing and not of any preassumed spatial wavelength. Therefore, the stability and appearance of the field (e.g., Figure 3) are not derived from classical smoothing, so discontinuities in the field will be preserved if they are resolved by the station spacing. The weighting is a function of distance, data uncertainty, and spatial structure function that is derived from the data itself. The method has properties akin to both median spatial filtering in image processing and geostatistical Kriging analysis, but least squares are not invoked (Hammond et al., 2016).

GPS Imaging is particularly useful for alignments between geodetic techniques in this case because tie points in the two data sets (e.g., GPS and leveling) are not always colocated, and there can be variable distance between a tie point and its nearest GPS station. To find the misfit field between the data sets, we use the algorithm to perform robust interpolation, not to a grid of values but from the locations of one method (e.g., GPS) onto the locations of the other (e.g., leveling). The robustness of the resulting differences make the shifting of one technique to another insensitive to outliers, account for uncertainties in the data, and give lower weight to ties with greater distance between them.

3.1.2. Tide Gauges Aligned With Leveling Lines

As part of the analysis described above we aligned the leveling and tide gauges together to check for consistency and remove the effects of leveling error at the 100 km scale (Burgette et al., 2009). This alignment is generally strong because the tide gauges have close ties to the leveling benchmarks as part of the network design. The coastal leveling route runs northwest from the Santa Monica tide gauge through Santa Barbara, to the Port San Luis tide gauge. We assume equal rates of geocentric sea level rise along this section of the coast, so that the negative of the relative sea level rise rates are the relative VLM rates between the gauges. Leveling-derived uplift rates referenced to the Port San Luis (PS) and Santa Monica (SM) tide gauges misfit the uplift rates from the discontinuous Santa Barbara tide gauge record by 2.2 and 2.8 mm/yr, respectively (with the Santa Barbara tide gauge uplift rate estimate exceeding the leveling uplift rate estimates). These misfits greatly exceed the combined uncertainties of 0.7 and 0.6 mm/yr, respectively. Further inspection of the local leveling conducted at the Santa Barbara tide gauge indicates that the primary benchmarks for different portions of the records were moving relative to one another at a vertical rate of ~ 1.2 mm/yr. The rate discrepancy between the relative tide gauge rates and relative leveling rates between the PS and SM tide gauges is 0.4 mm/yr (with the tide gauge estimate indicating a greater uplift rate of PS relative to SM), within the 1 sigma propagated uncertainty estimate of 1.0 mm/yr (combined leveling and tide gauge rate uncertainties). In light of these observations, we choose to reference the leveling rates to the relative tide gauge rates derived from the longer, more continuous records at the PS and SM tide gauges. The leveling rates are aligned to the tide gauge rates by both shifting and tilting over run distance in a weighted mean adjustment (Burgette et al., 2009), with weights determined from distance-dependent leveling uncertainties and the tide gauge rate analysis.

3.1.3. Leveling Aligned with GPS

In the next step we add a geographically uniform shift to the rates of the 201 leveling stations plus four tide gauges so that the rates reflect measurement of VLM in NA12. To estimate the size of the shift we interpolate the vertical GPS velocities to the location of the leveling stations using GPS Imaging as described above. We estimate the shift by taking the weighted median of the difference between leveling and GPS Imaging vertical

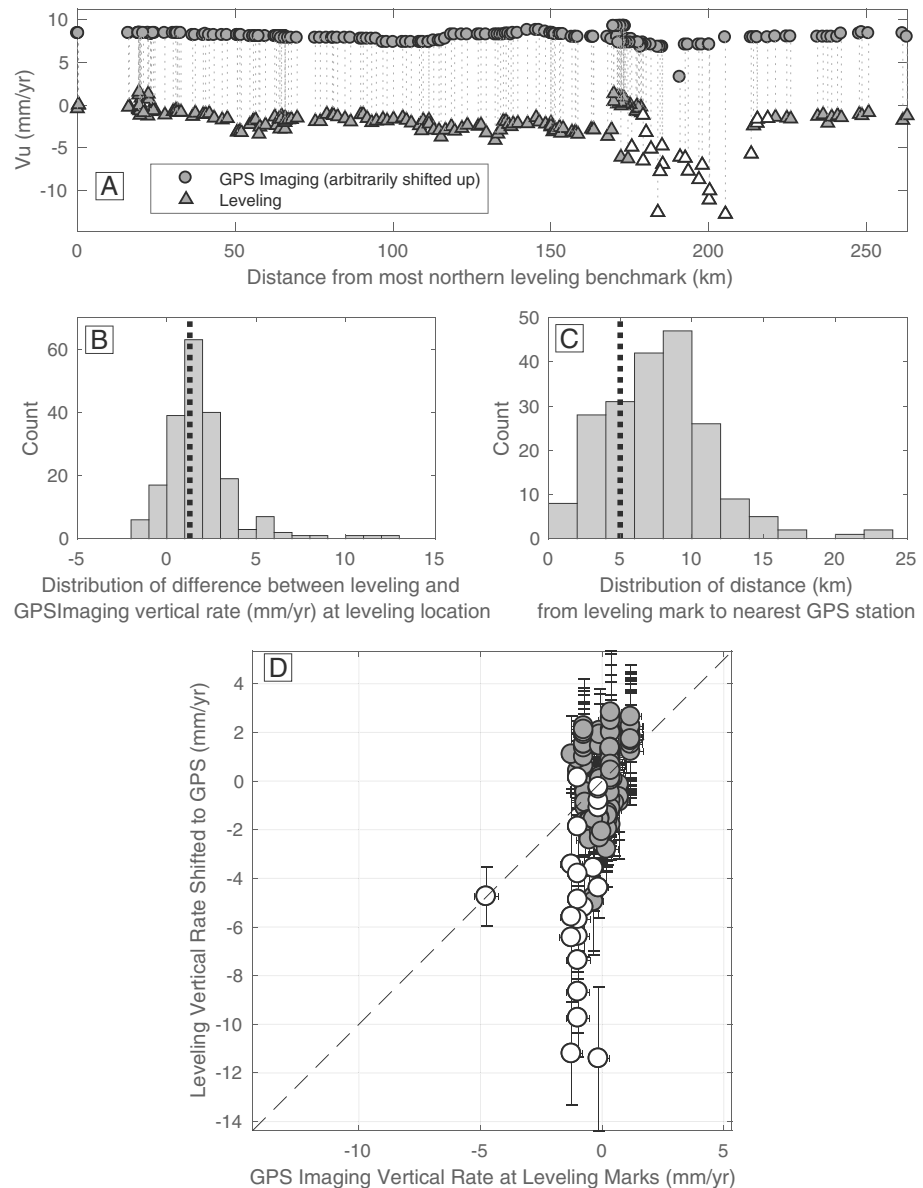


Figure 5. (a) Vertical rates from leveling line and GPS Imaging estimates of vertical rate at location of leveling benchmarks. GPS rate is shifted upward arbitrarily for figure clarity. (b) Histogram of difference between GPS Imaging (without arbitrary shift) and leveling rates in mm/yr. Weighted median value is shown with dashed vertical line. (c) Histogram of the distance between each leveling benchmark and the nearest GPS station. Dashed line indicates distance to nearest GPS station inside which a leveling station was used for alignment of leveling to GPS. (d) Scatter plot of GPS Imaging vertical rates at leveling stations versus leveling vertical rates after shifting into GPS reference frame. Uncertainties in the rates are 2σ . Diagonal dashed line indicates where GPS and leveling rates would be equal.

rates (Figure 5). Because the leveling data are more geographically dense than the GPS stations and follow coastal highway routes, they tend to sample areas of known rapid subsidence in, e.g., the Oxnard Plain of the Ventura Basin. In these locations we expect a poor fit between leveling and GPS because the nearest GPS station may be on an adjacent mountainside or other more stable locations. We address this spatial component of misfit in two ways. First, in calculating the shift between leveling and GPS we limit the data to leveling stations to within 5 km of a GPS station with a vertical rate, reducing the number to 47 locations. Second, we use a weighted median to estimate the shift, which guards against the bias introduced by the presence of a few large outliers in vertical rate difference between the two techniques. The resulting shift applied uniformly to the leveling rates is upward 1.29 mm/yr.

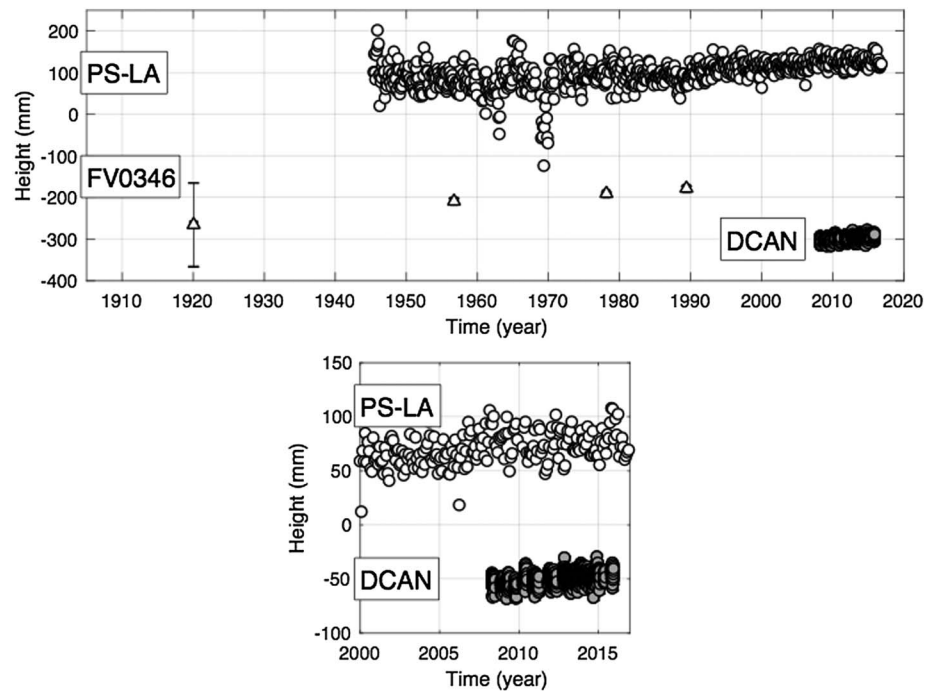


Figure 6. (top) Comparison between time series of height from different techniques. Time series of tide gauge measurements based on data from Port San Luis (PS) differenced with data from Los Angeles (LA) flipped and trend adjusted to represent crustal motion in NA12 (white circles). Leveling time series from benchmark FV0346 nearest to PS (white triangles with uncertainty bars) with trend adjusted to represent crustal motion in NA12. Time series of height of nearest GPS station to PS DCAN (gray circles). Data are shifted arbitrarily for plot clarity. (bottom) Close up of top plot for years 2000 through 2017.

The relationship between the shifted leveling rates and GPS Imaging interpolated rates is shown in Figure 5d. The median uncertainty in the leveling rates is 0.72 mm/yr, while the RMS difference between leveling and GPS rate is 2.10 mm/yr, where the leveling rates vary from -11 to 3 mm/yr. This is an indication that the leveling rates record larger variations in vertical rate than do the GPS data near the Ventura basin (Figure 5a) and record significant signal that is not present in the GPS velocity field. This can be seen in the leveling stations that subside more rapidly than the nearest GPS stations (rates near -11 mm/yr in Figure 5), particularly those that lie on the Oxnard Plain (colored white in Figure 5d), which is without direct GPS observation but has been shown with InSAR to be subsiding (Marshall et al., 2013). Where they are colocated, the aligned leveling time series have similar trends to nearby GPS stations even though they are measured over different times and time spans. This suggests that they both measure the same secular VLM (Figure 6). Including the aligned leveling with the GPS data in the GPS Imaging analysis significantly enhances geographic resolution of coastal subsidence compared to the GPS-only analysis (Figure 3b).

3.1.4. Tide Gauges Aligned With GPS

Since tide gauge rates are tied to the leveling during the analysis, the same 1.29 mm/yr shift is applied to the tide gauges (after flipping the tide gauge rates so they represent VLM with respect to sea surface). As a check we estimate how well the aligned vertical rates at tide gauges compare to GPS Imaging rates at the tide gauge locations (Figure 7a). The relationship indicates that the Santa Monica and Port San Luis tide gauges experience VLM that is to within uncertainty the same as the rate estimated using GPS Imaging. Also where they are colocated with GPS, the flipped and shifted tide gauge time series show similar trends (Figure 6). However, for the Santa Barbara and Los Angeles tide gauges, the rates are just significantly greater than the GPS Imaging rates, though the differences are small, less than 1 mm/yr in each case. One interpretation is that geographic variation of VLM contributes to greater rates at the tide gauges compared to expectation based on the nearest GPS stations by <1 mm/yr. In this case the addition of the tide gauges adds significant new information to the vertical rate field by constraining VLM at new locations. However, the disagreement between tide gauge and interpolated vertical GPS rates is not a strong function of distance between their locations (Figure 7b). One possibility is that VLM varies at the <1 mm/yr level over shorter distances than

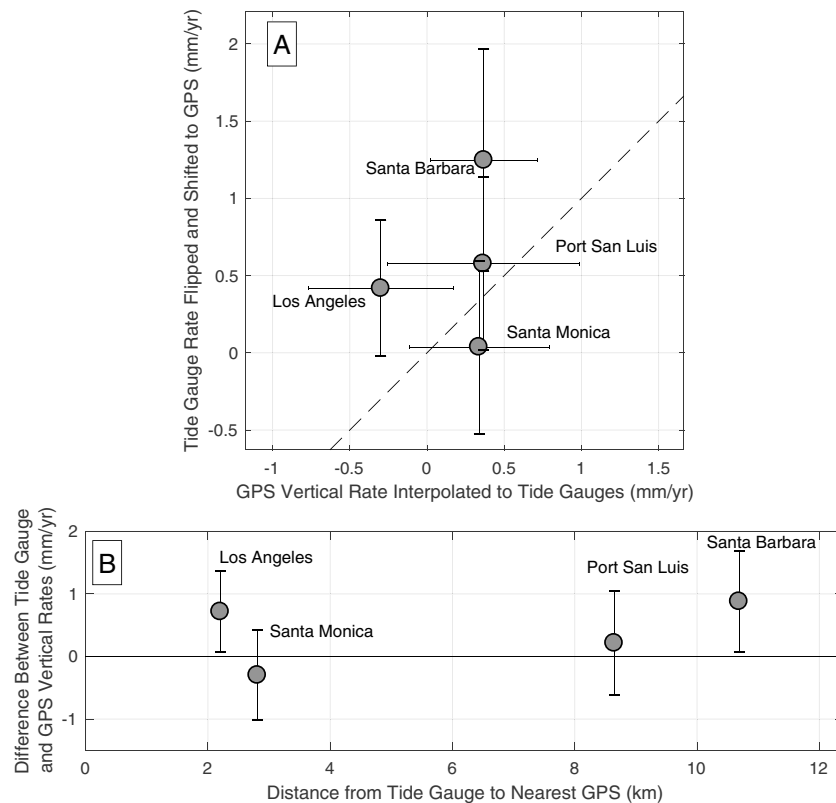


Figure 7. (a) Tide gauge rates, flipped and shifted to agree with interpolated GPS vertical rates. Uncertainties in the tide gauge rates are 2σ . Uncertainties in interpolated GPS vertical rates are a lower bound on the 2σ uncertainty, see text for discussion. Diagonal dashed line indicates where GPS and tide gauge rates would be equal. (b) Difference between tide gauge vertical rate and interpolated GPS vertical rate as a function of distance between tide gauge and nearest GPS station. Uncertainties (2σ) are the square root of the sum of squares of GPS and tide gauge vertical rate uncertainties.

the space between stations. Such short wavelength variation of VLM has been observed between some tide gauge benchmarks over 10^2 m length scales elsewhere (Burgette et al., 2009). It is also possible that reasons unrelated to VLM are behind the differences, for example, oceanographic trends that are not constant among the tide gauges (e.g., Stammer et al., 2013), factors influencing nearby GPS stations, or other contribution that make the actual uncertainties greater than we find in our analysis. Installation of GPS stations at the tide gauges, and collecting long observation records, would be particularly beneficial to resolving these matters and refining these alignments.

3.1.5. InSAR Aligned with GPS

In this step we bring the InSAR LOS rate images into the GPS reference frame. Owing to the various uncertainties in radar data processing and imaging, InSAR line of site rate maps are well known to have errors in the longest wavelength signals within the scenes. These errors can be conveniently addressed through a combination with GPS data since GPS networks are widespread, the data are easy to access and have the most precise vertical rates available (e.g., Gourmelen et al., 2010; Tong et al., 2013; Wei et al., 2010). We project the three-component GPS velocity into the radar line of site direction at each GPS site given the mission/track/frame look geometry obtained from the SAR satellite orbits, allowing for the variation of the look direction within each scene. Since the LOS is close to vertical, this step can be performed only with GPS velocities that have stable vertical rates, which we have ensured by using our stringent selection criteria in section 2.1. We sample the radar LOS rate field at the GPS station locations and estimate a median InSAR LOS rate inside a circle of radius 0.5 km.

We then minimize the misfit between the InSAR and GPS rates in the LOS direction by estimating and subtracting a misfit field using GPS Imaging. We use this transformation instead of a linear or quadratic estimate of an error ramp because we assume that long wavelength differences between InSAR and GPS are primarily attributable to errors in the InSAR rate maps. Thus, the InSAR is expected to add only

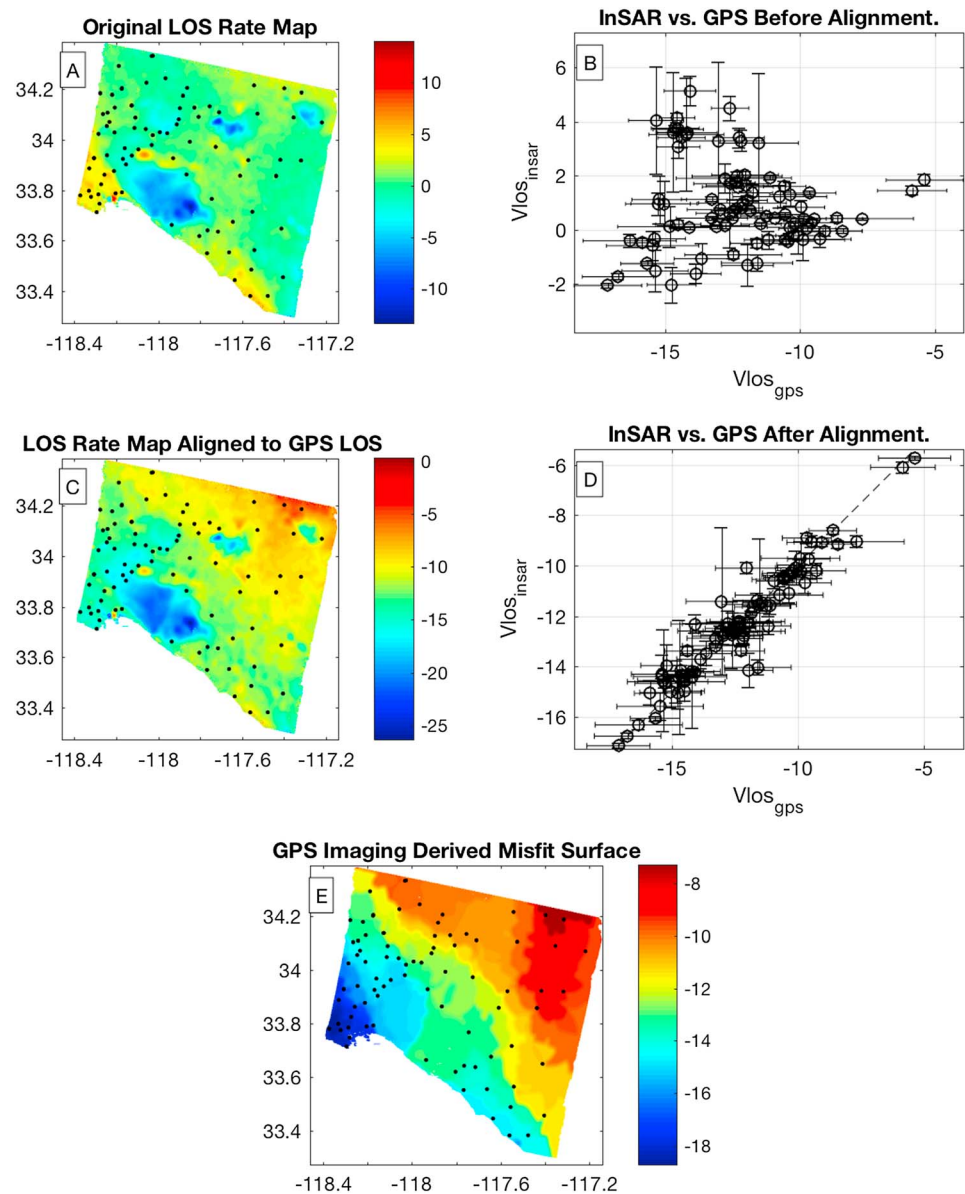


Figure 8. Example for Envisat track 170, frame 2925 showing the relationship between the GPS and InSAR LOS rates before and after the alignment is applied. (a) InSAR LOS before alignment, (b) relationship between InSAR and GPS LOS rates at GPS stations before alignment, (c) InSAR LOS after alignment, (d) relationship between InSAR and GPS LOS rates at GPS stations after alignment, (e) misfit surface determined by GPS Imaging that is the difference between Figures 8a and 8c. In Figures 8a and 8c black dots are locations of GPS stations. Color scale is set automatically in each panel to reflect range of data and is chosen to be different than the -3 to 3 mm/yr color scale we use for vertical motion.

signals with wavelengths near or less than the GPS station spacing. This is similar to the remove/filter/restore strategy of, for example, Wei et al. (2010) and Tong et al. (2013) except that GPS Imaging is not a spectral-based method and removes all disagreement between InSAR and GPS, though it derives a robust field that is insensitive to outliers in the misfit field. Figure 8 shows an example of the adjustment for Envisat track 170, frame 2925, and the rates before and after the alignment is applied, and these are shown for all track frames in the supporting information. After alignment, the RMS difference between InSAR and GPS LOS rate is ~ 1 mm/yr.

To compensate for the effects of horizontal interseismic crustal motion, we remove from each LOS rate field the expected contribution from horizontal motion. To estimate this we use the MIDAS horizontal GPS velocities projected into the local LOS and interpolate them onto a grid using GPS Imaging. We use the same

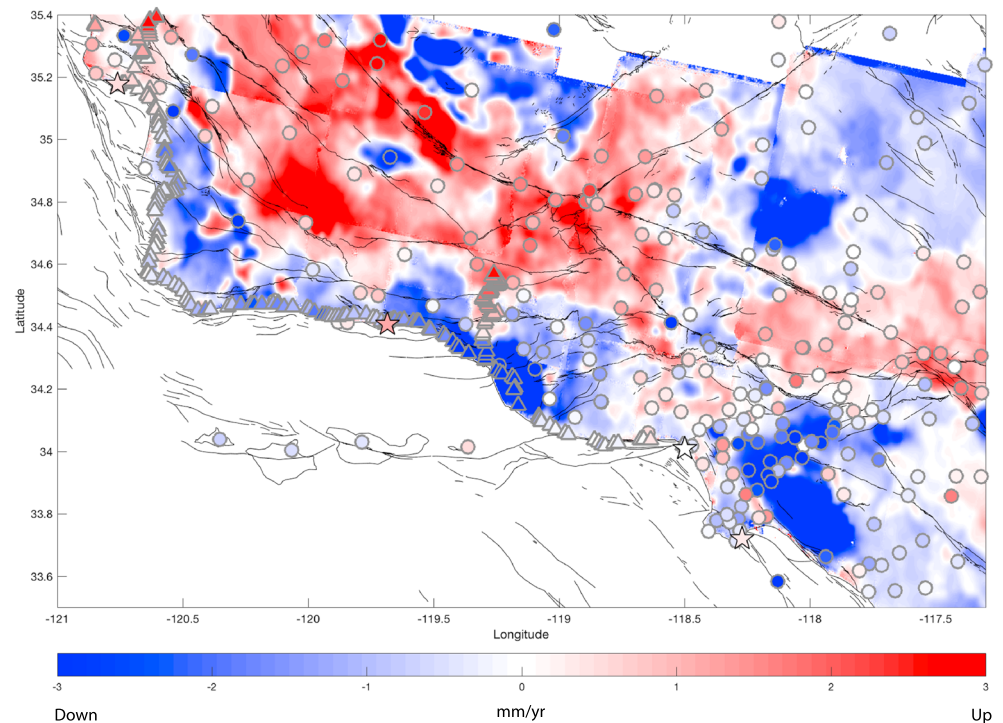


Figure 9. Mosaic of aligned InSAR (background color map), GPS (gray outlined circles), leveling (gray outlined triangles), and tide gauges (outlined stars). Internal color of symbol shows vertical rate with same color scale in mm/yr for all techniques, red is up and blue is down. Black lines show faults from the USGS Quaternary Fault and Fold Database (USGS & CGS, 2006).

ground to satellite look vector fields used in the previous section and subtract the projected signal from the LOS rate map. What remains is an estimate of the LOS component of the signal attributable to vertical ground motion. We project the LOS to estimate vertical motion using the angle between vertical and the ground to satellite look vector $\theta(x,y)$:

$$v_{up}(x,y) = v_{LOS}(x,y) / \cos(\theta(x,y)) \quad (1)$$

where x and y are latitude and longitude, respectively. The look directions for the ERS and Envisat scenes are between 19° and 27° from vertical. Thus, scaling of v_{LOS} to get v_{up} is small, about a factor of between 1.058 and 1.122.

3.1.6. Mosaicking InSAR

In the final step, we make a mosaic by shifting the individual InSAR vertical rate track/frame maps to minimize misfit between the rates from GPS and the leveling and tide gauges. Though the InSAR rates were already transformed into the GPS LOS reference frame, this final alignment step is prudent because it is constrained by vertical rates from all three of the techniques (i.e., leveling and tide gauges are added in) and results in less pronounced discontinuities at the seams between overlapping radar scenes. We order the scenes to maximize overlap during mosaicking iterations by first selecting the scene with the strongest distribution of GPS + leveling + tide gauge locations to constrain the alignment, in this case the ERS track 442 frame 2907 (Figure 1). We then select the next mission/track/frame that has the greatest amount of overlap with the mosaic in the previous step, aligning and merging iteratively until all scenes are included. To minimize disagreement at the InSAR scene seams, the alignment misfit surface is derived from all techniques including InSAR data already in the mosaic from previous iterations. The result (Figure 9) shows notable agreement between the techniques, indicating that the alignments are successful in removing long wavelength errors in the InSAR data. Some zones of subsidence indicate that downward motion is resolved independently in InSAR and GPS (e.g., in the Cuyama Valley near latitude 34.9° , longitude -119.6°). Other examples include agreement in downward motion in the Los Angeles, Ventura, San Joaquin, and Antelope basins in the western Mojave, and in uplift west of the SAF.

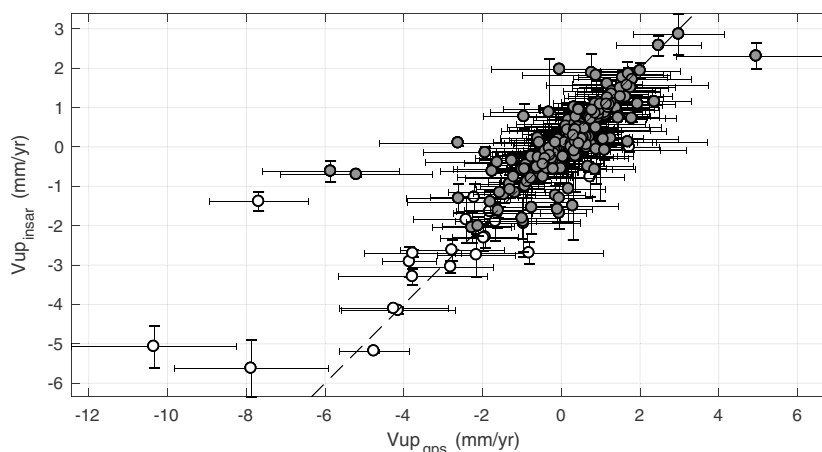


Figure 10. Scatterplot of vertical GPS velocity compared to vertical velocity inferred from InSAR data within 0.5 km of the GPS station. White circles are stations that lie within areas defined by the nontectonic motion mask in Figure 12. RMS difference between GPS and InSAR vertical rates is 0.97 mm/yr before and 0.92 mm/yr after masking. Uncertainties in the rates are 2σ .

The mosaic provides greater detail that fills in gaps between the GPS stations; much of the precision and stability of the long wavelength features in the vertical rate field come from GPS which experiences little error in long wavelength signal. Comparing the uplift pattern in Figure 9 to the GPS-only signal in Figure 3a shows that the long wavelength features seen in GPS are preserved in the multitechnique mosaic, including the uplift of the WTR. However, between GPS stations the rate and delineation of boundaries of subsidence are improved by adding InSAR.

The weakest location in the alignment may be just inland from the coast near longitude -120.5° and between latitude 34.6° and 35.2° , north of Point Conception, where we only have a single descending LOS track/frame set, as we were not able to get a large number of coregistered scenes for Envisat track 256/2907. Short wavelength signals that alternate between positive and negative become more obvious here, because they are near a change in color scale polarity from blue to red. Furthermore, GPS coverage is relatively poor here (several recently added stations do not yet have long enough time series to pass our exclusion criteria), so there is greater uncertainty in the uplift field in this location.

The degree to which the InSAR vertical rates agree with GPS after alignment is shown in Figure 10. We compare the vertical GPS rates to the InSAR rates by taking the mean vertical InSAR rate inside a circle of radius 0.5 km around each GPS station. The uncertainty in the GPS is derived from the MIDAS velocities and the uncertainty in the InSAR rates is estimated from the RMS scatter of InSAR rates within the 0.5 km circle. The RMS difference between GPS and InSAR rates is 0.97 mm/yr, similar in size to the maximum uncertainty in the GPS velocities used in this analysis (Figure 2c), which we take as a measure of the uncertainty in the aligned InSAR rate field. The scatterplot in Figure 10 suggests that the greatest misfits between InSAR and GPS are at the stations that are subsiding fastest. These locations tend to be those experiencing nontectonic effects in basins affected by groundwater or hydrocarbon extraction (Argus et al., 2005; Bawden et al., 2001; Marshall et al., 2013; Watson et al., 2002). They also have the greatest changes in their rates over time, as climate and aquifer management influences the rate of groundwater-related subsidence. Generally, when the misfits are largest the GPS rates are subsiding faster compared to the InSAR rates. This may be because InSAR time series go back to 1992, while all GPS data we consider were collected after 1996 and most were collected after 2005 (Table 1). This is consistent with subsidence rates that increased over time, with GPS seeing faster rates of subsidence in the later period over which they were collected.

An additional measure of uncertainty in the InSAR occurs where overlap in the scenes generate visible discontinuities. These areas of overlap are an ongoing issue with creating mosaics of InSAR scenes since different error sources combine to create them (Shirazaei, 2015). Our analysis corrects for look angle effects so the seam discontinuities are likely errors from, for example, atmosphere, that have a mismatch in adjacent track/frame sets, so the magnitude of the steps can provide insight into the size of these errors. The size of

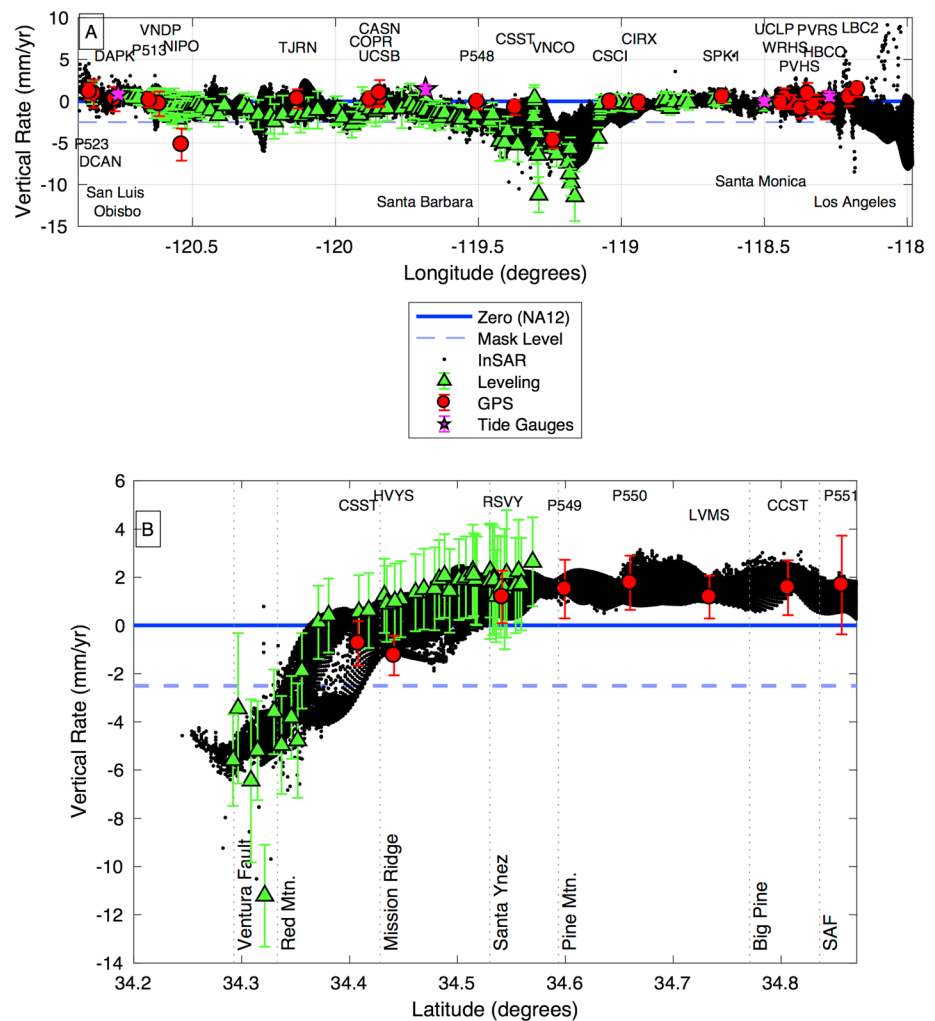


Figure 11. (a) Coastal profile of vertical velocities given by all four measurement techniques within 10 km of coastline aligned to common reference frame. Text below data indicates tide gauge locations. (b) Ojai profile, vertical rate as function latitude from coast to San Andreas Fault. Uncertainty bars plotted are 2σ . The four-character ID of GPS stations are shown above their location. The horizontal blue bar indicates zero vertical velocity in the NA12 reference frame. The light blue horizontal dashed bar indicates the mask level (see text and Figure 12).

discontinuities in the vertical rates across seam boundaries vary from zero to ~ 1 mm/yr. Thus, while these seams are quite clear to the human eye, they are consistent with the overall error in the InSAR rate field and hence are mostly not significant.

3.2. Vertical Rate Field Uncertainty

The median aleatory rate uncertainties are 0.23 mm/yr for tide gauges, 0.51 mm/yr for GPS, 0.72 mm/yr for leveling, and ~ 1 mm/yr for InSAR. Comparisons between the techniques, however, provide a more inclusive measure of uncertainties because they reveal contributions not found in the formal uncertainties of individual techniques. When, for example, rates from separate techniques at the same location differ slightly, it may be because they measure motion over different times. In this case the intertechnique comparisons more fully reflect the uncertainty in the long-term steady component of motion attributable to tectonic deformation. However, those comparisons can overstate uncertainty because the different techniques are not always perfectly colocated. Thus, the single technique uncertainties are lower bounds, and comparisons are upper bounds. In Figure 11 we show profiles of all four techniques plotted together along the coast from Port San Luis to Los Angeles, and along the inland Ojai profile. The uncertainties are shown with error bars for the GPS, leveling, and tide gauge data. In most cases the different methods plot within the error bounds

or scatter of the other techniques, with some exceptions (e.g., the GPS station NIPO, near -120.58° longitude in Nipomo, CA subsides at -5.2 ± 1.0 mm/yr, outside the range of the nearest leveling, InSAR, and tide gauge measurements). The uncertainties are small enough to preserve the signals of uplift, while being large enough to reckon broad agreement between techniques.

A separate indicator of the stability of the imaging is the similarity between the histograms of InSAR and GPS-derived signals (Figure 2). Both the InSAR and GPS distributions exhibit a hump on the right and a long tail on the left. The hump reflects the part of the landscape experiencing interseismic surface uplift. The tail on the left indicates the relatively fast downward motion owing to nontectonic subsidence in basins, discussed in the next section. The similarity between the distributions suggests (1) that both are sampling the same underlying field of vertical motion of Earth's surface, regardless of source, despite the fact that the two data sets are collected over slightly different periods of observation and/or (2) the aligned InSAR rates adopt the long wavelength uplift signal of the GPS but also preserves the subsiding areas that give it the long tail. This suggests that the underlying rate field responsible for these features is steady over the periods covered by both sets of observations.

3.3. Separation of Tectonic Versus Nontectonic Signals

One goal of this research is to derive a vertical rate field that constrains interseismic tectonic deformation and fault slip rates (Johnson et al., 2014; Marshall et al., 2017). For that application areas that represent nontectonic deformation should be removed. We see rapid subsidence in the Ventura basin, Los Angeles basin, Cuyama Valley, Chino Valley, Antelope Valley in the western Mojave Desert, and southern San Joaquin Valley, that are likely related to groundwater changes and in some cases hydrocarbon pumping (Figure 9). In most cases subsidence is more rapid in absolute terms than uplift, occupying the left tail in Figure 2. In many cases the boundaries of the basin-related signals are sharp and are fault controlled, as seen in previous studies (Argus et al., 2005; Bawden et al., 2001; Watson et al., 2002; Wisely & Schmidt, 2010). We find, like Lanari et al. (2004) and Brooks et al. (2007) variable uplift/subsidence along the coast near Los Angeles and Palos Verdes and uplift between Downy and La Habra possibly associated with fluid recharge under an exceptionally high concentration of historical oil wells (CA Department of Conservation, Division of Oil, Gas, & Geothermal Resources, 2016). In the San Joaquin Valley the InSAR outlines complicated patterns of subsidence known to be associated with aquifer withdrawal (Farr & Liu, 2015; Sneed et al., 2013; U.S. Geological Survey California Water Science Center (USGS CWSC), 2017).

We separate nontectonic from tectonic signals using a masking approach based on geodetic signal characteristics. Areas subject to groundwater withdrawal tend to be areas with rapid subsidence and larger amplitude of annual motion (Amos et al., 2014; Argus et al., 2005; Bawden et al., 2001; Lanari et al., 2004). We create a mask by selecting areas of the rate field that subside more quickly than -2.5 mm/yr and have annual terms of oscillation from InSAR or an interpolation of the annual terms in the GPS time series larger than 2.0 mm. We use GPS Imaging to estimate annual terms at every point on the grid (Figure 12). The mask covers $\sim 8\%$ of the figure and omits areas in the southernmost San Joaquin Valley, western Mojave, coastal Ventura basin, and a substantial portion of the Los Angeles basin. Masked areas are very similar to those shown on the USGS online subsidence map (USGS CWSC, 2017). In Figure 10 the effect of the mask on which data are omitted is shown by coloring points within the mask white, which confirms that areas with the most negative rates and greatest misfit between InSAR and GPS, are masked out. A few GPS stations moving downward over 5 mm/yr remain unmasked, suggesting that the mask is conservative and could be extended more to exclude more of the area as moving nontectonically. While much of the downward moving areas are associated with aquifers, some of the subsidence may be tectonic in origin (Nicholson et al., 2007; Pinter et al., 2003; Sorlien et al., 2013), so we do not want the mask to remove all areas of subsidence too aggressively.

4. Results and Discussion

The mosaic shown in Figures 9 and 11 shows that the rates and patterns of contemporary VLM are geographically coherent, agree between techniques, and are characteristic of the interseismic signal associated with contraction across thrust faults around the Ventura area and WTR. The consistency of the most rapid signals seen in both the terrestrial and satellite data, notably subsidence of the Ventura basin and uplift of WTR (Figures 9 and 11), indicate that these movements persist over much of the past century. Likewise, the

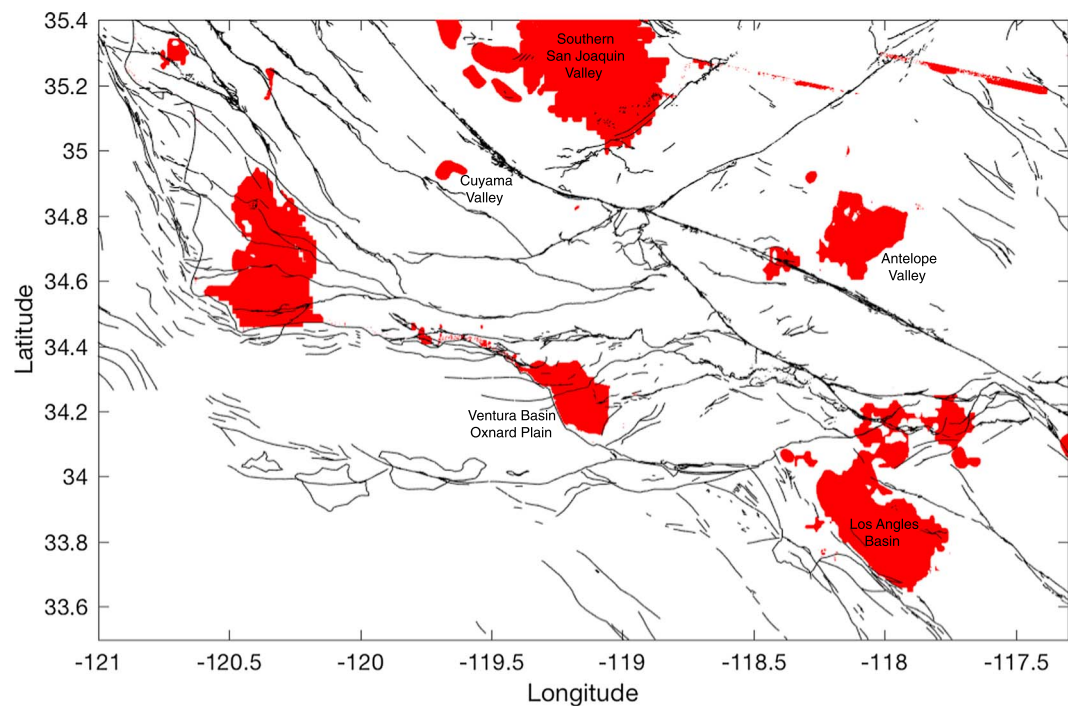


Figure 12. Areas with red shading are those identified in the analysis as having nontectonic motions. These areas include the groundwater aquifers in the Los Angeles basin, southern Great Valley of California, western Mojave Desert, westernmost Ventura Basin, plus a number of other smaller areas with isolated nonlinear behavior and show a strong resemblance to known ground water subsidence features (see https://ca.water.usgs.gov/land_subsidence/california-subsidence-areas.html, USGS CWSC, 2017).

linear trends of tide gauges are consistent with VLM rates being steady over the past century at the tide gauge locations (Figure 6). The observed compatibility of data collected with very different techniques over nonoverlapping time periods (in the case of leveling versus satellite data) suggests that the rate field reflects processes that are long lived and associated with tectonics and the earthquake cycle.

Most obvious to the eye is the signal of gradually varying 1–2 mm/yr uplift west of the San Andreas Fault (SAF) extending about half way to the coast between Santa Monica and Port San Luis (Figure 9). The upward signal is remarkably continuous along strike with the SAF, extending from the Coast Ranges to the north, through the WTR north of the Santa Barbara channel, connecting southward to a wedge-shaped zone of ~1 mm/yr uplift between the SAF and San Gabriel/Sierra Madre fault system. This section of the uplift field is centered and roughly limited to the extent of the crustal block that includes the San Gabriel Mountains, with a slight gap in the pattern near the Soledad and Clearwater faults. Here the uplift is highly asymmetric across the Mojave section of the SAF, upward on the west side and zero downward on the east side. In the Mojave Desert the motion is consistently downward at a rate of –1 to 0 mm/yr that extends as far as the eastern limit of our study area (longitude –117.3°). The approximate location of the Garlock fault bounds the Mojave subsidence to the north, similar to the findings of Fay et al. (2008). We also see ~0.5 mm/yr of uplift on the eastern Santa Monica Mountains, suggesting that interseismic uplift is active north of the Hollywood and Santa Monica faults, similar to geologic rates tabulated by Niemi et al. (2008). Throughout the study area there are some similarities to the observations of Howell et al. (2016), for example, uplift in the Coast Ranges and western WTR. However, our observations are different in the Mojave where they observed uplift, and we see subsidence (more similar to their physical model). Compared to the vertical GPS rates of Marshall et al. (2017), which have a maximum near 1 mm/yr, we find slightly higher maximum rates (~2 mm/yr) with more spatially continuous uplift in our mosaic (Figures 9 and 11) compared to their interpolation of GPS rates. In the southern Mojave Desert (near longitude –117.4°) our uplift field begins to bleed across the east side of the SAF near the San Bernardino Mountains where the high topography of the WTR also flips over to the east side of the fault. Branching off the SAF near the Big Bend, a band of uplift extends northeast, between the Garlock and White Wolf fault zones.

Uplift patterns we observe coincide with features in some other data that bear on the physical state of the Earth's crust in southern California. For example, there is a similarity between the pattern of uplift and the distribution of high topography and active faulting; the WTR experience uplift, while the lower lying areas such as the Oxnard Plain and much of the Mojave Desert move downward. The areas of uplift tend to have denser concentrations of microseismicity, for example, west of the SAF, in the San Bernardino Mountains east of the SAF, in the Transverse Ranges, and between the Garlock and White Wolf Fault north of the Mojave Desert (Hardebeck & Hauksson, 2001), suggesting they may be under greater crustal stress. There is also a similarity between the locations of uplift and (1) the highest magnitude horizontal crustal strain rate (e.g., Kreemer et al., 2012; Shen et al., 1996), (2) locations of earthquakes with a predominance of thrust mechanism style of faulting (U.S. Geological Survey and California Geological Survey, 2006), (3) locations with high misorientation between crustal strain rate and stress orientation (Yang & Hauksson, 2013), and (4) greater crustal thickness (Fuis et al., 2001; Kohler & Davis, 1997). Together, the observations are plausibly consistent with the vertical rate field being an effect of active crustal shortening, with the SAF acting as a near-vertical buttress keeping contraction to the southwest of the SAF.

An additional observation suggests that the observed uplift field is primarily a feature of WTR crustal contraction. The compilation of Niemi et al. (2008) shows that long-term uplift rates at the Santa Barbara coast exceed 1 mm/yr, whereas the interseismic velocities (Figures 9 and 11) show mostly subsidence from the Santa Monica Mountains through west of Santa Barbara. The north-south profile crossing these faults (Figure 11) indicates that InSAR, leveling and GPS agree on this downward-toward-the-coast gradient (Figure 11b), where subsidence rates are as fast as -1 mm/yr. Reconciling the disagreement between long-term uplift and interseismic subsidence with north-south crustal contraction is characteristic of fault-based models of the earthquake cycle that includes backslip in the shallow locked region (Freund & Barnett, 1976; Huang et al., 2010; Savage, 1983). In these models the maximum uplift rate occurs above the bottom of the locked section and results in downward elastic flexing on the footwall side of the fault (Johnson et al., 2014; Marshall et al., 2013). For the thrust faults in the Ventura area and Santa Barbara channel that accommodate contraction across the WTR, for example, Red Mountain, Ventura and San Cayetano Faults (Figure 1), the maximum uplift is predicted to be north of the fault traces by ~ 20 km, near the observed maximum in our uplift field. Offset of the most rapid uplift well to the north of the surface trace of the Ventura-Pitas Point fault system is consistent with observations and modeling of Marshall et al. (2017) and supports the existence of a ramp-flat geometry at depth. The greater along-strike continuity of this area of rapid interseismic uplift imaged here suggests that the deeper crustal ramp may be continuous to the east, downdip of the San Cayetano fault. A large, connected fault ramp underlying these structures has been argued on structural grounds (Hubbard et al., 2014), and the continuity of rapid interseismic uplift is consistent with large magnitude vertical paleo-earthquake displacements on these faults (McAuliffe et al., 2015; Rockwell et al., 2016).

The effect of elastic crustal rebound associated with groundwater withdrawal contributing to uplift signals in California has been recognized previously (Amos et al., 2014; Borsa et al., 2014; Holzer, 1979). It is likely that hydrological unloading attributable to aggressive groundwater pumping during the California drought period (2011–2016) drives some of the uplift around the perimeter of the San Joaquin Valley (SJV). However, it is unlikely that groundwater unloading from the SJV extend as far south as the southern end of the San Gabriel block and beyond, the extent of the observed uplift. Furthermore, the correlation of the uplift with the boundaries of the WTR and San Gabriel block, and the consistency between short-term and long-term geodetic observations, together suggest that the uplift is a longer-term response to plate boundary tectonics expressed through interseismic earthquake cycle deformation.

5. Conclusions

We combine four geodetic techniques to obtain a map of contemporary bedrock VLM across the WTR of southern California. The geodetic techniques have complementary strengths, with the precision and global reference frame from GPS, blanket coverage from InSAR, and decades long observation from leveling and tide gauges. We create a mosaic of VLM using ties between the techniques and the GPS Imaging algorithm for robust median-based estimation to minimize the intertechnique misfits. The uncertainty in the rate field is ~ 1 mm/yr.

The results of the alignments show coherent patterns of VLM across the WTR associated with interseismic uplift and strain accumulation on active thrust faults, revealing important features of deformation of the lithosphere. The uplift is highly asymmetric across the Mojave section of the SAF, with areas east of the fault moving downward as fast as 1 mm/yr and areas west of the fault moving upward 1–2 mm/yr. This uplift feature follows the SAF throughout our study area, extending from the San Bernardino Mountains to the central California Coast Ranges, down dip of the traces of major WTR faults. Everywhere along this uplift zone the VLM trends downward toward the Pacific coastline. The signals associated with groundwater basins do not represent long-term tectonic deformation and can be recognized from their high rates of, or time variability of, subsidence. We use these features to create a mask to filter out nontectonic deformation to emphasize uplift patterns that reveal active processes deforming the WTR crust. We conclude from the relationship between uplift with the faults and boundaries of the WTR and San Gabriel block, and the consistency between short term and long-term geodetic observations, that the uplift represents interseismic deformation across thrust faults in the Ventura area and Santa Barbara channel that accommodate contraction across the WTR.

Acknowledgments

We thank UNAVCO for GPS data collection, data archiving, distribution, and hosting of software products for the EarthScope Plate Boundary Observatory and GAGE Facility, supported by the National Science Foundation awards EAR-0350028, EAR-0732947, and EAR-1261833. We thank the operators of the other GPS networks whose data were used in this study including SCIGN, BARD, and CORS in southern California. We thank the Jet Propulsion Laboratory for the GIPSY software and for data products used in the GPS data processing. The European Space Agency collected the InSAR data, which we obtained from the WinSAR archive hosted by UNAVCO. The InSAR analysis was performed with software from Gamma Remote Sensing using the satellite orbit products from Delft University. We obtained SRTM data from the USGS (<http://dds.cr.usgs.gov/srtm/>). We obtained leveling and tide gauge data from NOAA who operates the instruments, archives, and distributes the data. We are grateful for collaborative support from SCEC project 14209 to W. C. H. and R. J. B., and from the National Science Foundation for the project "Revealing the Nature of Contemporary Uplift and Collapse in the Sierra Nevada-Great Basin System" (awards 0844389 and 1252210) to G. B. and W. C. H. W. C. H. and G. B. also received support from the NASA ROSES Sea Level Change Team program projects NN14AJ98G and 80NSSC17K0565. This research was supported by the Southern California Earthquake Center (contribution 8006). SCEC is funded by NSF cooperative agreement EAR-1033462 and USGS cooperative agreement G12AC20038.

References

- Altamimi, Z., Collilieux, X., & Métivier, L. (2011). ITRF2008: An improved solution of the international terrestrial reference frame. *Journal of Geodesy*, 85(8), 457–473. <https://doi.org/10.1007/s00190-011-0444-4>
- Amos, C. B., Audet, P., Hammond, W. C., Bürgmann, R., Johanson, I. A., & Blewitt, G. (2014). Uplift and seismicity driven by groundwater depletion in central California. *Nature*, 509(7501), 483–486. <https://doi.org/10.1038/nature13275>
- Argus, D. F., Heflin, M. B., Peltzer, G., Crampé, F., & Webb, F. H. (2005). Interseismic strain accumulation and anthropogenic motion in metropolitan Los Angeles. *Journal of Geophysical Research*, 110, B04401. <https://doi.org/10.1029/2003JB002934>
- Bar Sever, Y. E., Kroger, P. M., & Borjesson, J. A. (1998). Estimating horizontal gradients of tropospheric path delay with a single GPS receiver. *Journal of Geophysical Research*, 103(B3), 5019–5035. <https://doi.org/10.1029/97JB03534>
- Bawden, G. W., Thatcher, W., Stein, R. S., Hudnut, K. W., & Peltzer, G. (2001). Tectonic contraction across Los Angeles after removal of groundwater pumping effects. *Nature*, 412(6849), 812–815. <https://doi.org/10.1038/35090558>
- Berardino, P., Fornaro, G., Lanari, R., & Sansosti, E. (2002). A new algorithm for surface deformation monitoring based on small baseline differential SAR interferograms. *IEEE Transactions on Geoscience and Remote Sensing*, 40(11), 2375–2383. <https://doi.org/10.1109/TGRS.2002.803792>
- Bertiger, W., Desai, S. D., Haines, B., Harvey, N., Moore, A. W., Owen, S., & Weiss, J. P. (2010). Single receiver phase ambiguity resolution with GPS data. *Journal of Geodesy*, 84(5), 327–337. <https://doi.org/10.1007/s00190-010-0371-9>
- Blewitt, G., Kreemer, C., Hammond, W. C., & Gazeaux, J. (2016). MIDAS trend estimator for accurate GPS station velocities without step detection. *Journal of Geophysical Research: Solid Earth*, 121, 2054–2068. <https://doi.org/10.1002/2015JB012552>
- Blewitt, G., Kreemer, C., Hammond, W. C., & Goldfarb, J. (2013). Terrestrial reference frame NA12 for crustal deformation studies in North America. *Journal of Geodynamics*, 72, 11–24. <https://doi.org/10.1016/j.jog.2013.08.004>
- Boehm, J., Niell, A., Tregoning, P., & Schuh, H. (2006). Global mapping function (GMF): A new empirical mapping function based on numerical weather model data. *Geophysical Research Letters*, 33, L07304. <https://doi.org/10.1029/2005GL025546>
- Borsa, A. A., Agnew, D. C., & Cayan, D. R. (2014). Ongoing drought-induced uplift in the western United States. *Science*, 345(6204), 1587–1590. <https://doi.org/10.1126/science.1260279>
- Brooks, B. A., Merrifield, M. A., Foster, J., Werner, C. L., Gomez, F., Bevis, M., & Gill, S. (2007). Space geodetic determination of spatial variability in relative sea level change, Los Angeles basin. *Geophysical Research Letters*, 34, L01611. <https://doi.org/10.1029/2006GL028171>
- Buchanan-Banks, J. M., Castle, R. O., & Ziony, J. I. (1975). Elevation changes in the central transverse ranges near Ventura, California. *Tectonophysics*, 29(1–4), 113–125. [https://doi.org/10.1016/0040-1951\(75\)90137-7](https://doi.org/10.1016/0040-1951(75)90137-7)
- Burgette, R. J., Watson, C. S., White, N. J., Church, J. A., Tregoning, P., & Coleman, R. (2013). Characterizing and minimizing the effects of noise in tide gauge time series: Relative and geocentric sea level rise around Australia. *Geophysical Journal International*, 194(2), 719–736. <https://doi.org/10.1093/gji/ggt131>
- Burgette, R. J., Weldon, R. J., & Schmidt, D. A. (2009). Interseismic uplift rates for western Oregon and along-strike variation in locking on the Cascadia subduction zone. *Journal of Geophysical Research*, 114, B01408. <https://doi.org/10.1029/2008JB005679>
- Bürgmann, R., Rosen, P., & Fielding, E. J. (2000). Synthetic aperture radar interferometry to measure Earth's surface topography and its deformation. *Annual Review of Earth and Planetary Sciences*, 28(1), 169–209. <https://doi.org/10.1146/annurev.earth.28.1.169>
- CA Department of Conservation, Division of Oil, Gas & Geothermal Resources (2016). Retrieved from <http://www.conservation.ca.gov>
- Chen, C. W., & Zebker, H. A. (2000). Network approaches to two-dimensional phase unwrapping: Intractability and two new algorithms. *Journal of the Optical Society of America*, 17(3), 401–414. <https://doi.org/10.1364/JOSAA.17.000401>
- Church, J. A., White, N. J., Coleman, R., Lambeck, K., & Mitrovica, J. X. (2004). Estimates of the regional distribution of sea level rise over the 1950–2000 period. *Journal of Climate*, 17(13), 2609–2625. [https://doi.org/10.1175/1520-0442\(2004\)017%3C2609:EOTRDO%3E2.0.CO;2](https://doi.org/10.1175/1520-0442(2004)017%3C2609:EOTRDO%3E2.0.CO;2)
- Costantini, M. (1998). A novel phase unwrapping method based on network programming. *IEEE Transactions on Geoscience and Remote Sensing*, 36(3), 813–821. <https://doi.org/10.1109/36.673674>
- Dolan, J. F., & Rockwell, T. K. (2001). Paleoseismologic evidence for a very large ($M_w > 7$), post-1660 A.D. surface rupture on the eastern San Cayetano fault, Ventura County, California: Was this the elusive source of the damaging December 21, 1812 earthquake? *Bulletin of the Seismological Society of America*, 91(6), 1417–1432. <https://doi.org/10.1785/0120000602>
- Dong, D., Fang, P., Bock, Y., Webb, F., Prawirodirdjo, L., Kedar, S., & Jamason, P. (2006). Spatiotemporal filtering using principal component analysis and Karhunen-Loeve expansion approaches for regional GPS network analysis. *Journal of Geophysical Research*, 111, B03405. <https://doi.org/10.1029/2005JB003806>
- Donnellan, A., Hager, B. H., & King, R. W. (1993). Discrepancy between geological and geodetic deformation rates in the Ventura Basin. *Nature*, 366(6453), 333–336. <https://doi.org/10.1038/366333a0>

- Farr, T. G., & Liu, Z. (2015). Monitoring subsidence associated with groundwater dynamics in the Central Valley of California using interferometric radar. In V. Lakshmi (Ed.), *Chapter 24 in Remote sensing of the terrestrial water cycle, Geophysical Monograph Series* (Vol. 206, pp. 397–406). Washington, DC: American Geophysical Union.
- Fay, N. P., Bennett, R. A., & Hreinsdóttir, S. (2008). Contemporary vertical velocity of the central basin and range and uplift of the southern Sierra Nevada. *Geophysical Research Letters*, 35, L20309. <https://doi.org/10.1029/2008GL034949>
- Federal Geodetic Control Committee (1984). *Standards and specifications for geodetic control networks, report*. Rockville, Md: Natl. Oceanic and Atmos. Admin.
- Freund, L. B., & Barnett, D. M. (1976). A two-dimensional analysis of surface deformation due to dip-slip faulting. *Bulletin of the Seismological Society of America*, 66(3), 667–675.
- Fuis, G. S., Ryberg, T., Godfrey, N. J., Okaya, D. A., & Murphey, J. M. (2001). Crustal structure and tectonics from the Los Angeles basin to the Mojave Desert, southern California. *Geology*, 29(1), 15–18. [https://doi.org/10.1130/0091-7613\(2001\)029%3C0015:CSATFT%3E2.0.CO;2](https://doi.org/10.1130/0091-7613(2001)029%3C0015:CSATFT%3E2.0.CO;2)
- Gazeaux, J., Williams, S., King, M., Bos, M., Dach, R., Deo, M., ... Webb, F. H. (2013). Detecting offsets in GPS time series: First results from the detection of offsets in GPS experiment. *Journal of Geophysical Research: Solid Earth*, 118, 2397–2407. <https://doi.org/10.1002/jgrb.50152>
- Goldstein, R. M., & Werner, C. (1998). Radar interferogram filtering for geophysical applications. *Geophysical Research Letters*, 25(21), 4035–4038. <https://doi.org/10.1029/1998GL900033>
- Gourmelen, N., Amelung, F., & Lanari, R. (2010). Interferometric synthetic aperture radar–GPS integration: Interseismic strain accumulation across the Hunter Mountain fault in the eastern California shear zone. *Journal of Geophysical Research*, 115, B09408. <https://doi.org/10.1029/2009JB007064>
- Hamlington, B. D., Thompson, P., Hammond, W. C., Blewitt, G., & Ray, R. D. (2016). Assessing the impact of vertical land motion on twentieth century global mean sea level estimates. *Journal of Geophysical Research: Oceans*, 121, 4980–4993. <https://doi.org/10.1002/2016JC011747>
- Hammond, W. C., Blewitt, G., & Kreemer, C. (2016). GPS imaging of vertical land motion in California and Nevada: Implications for sierra Nevada uplift. *Journal of Geophysical Research: Solid Earth*, 121, 7681–7703. <https://doi.org/10.1002/2016JB013458>
- Hardebeck, J. L., & Hauksson, E. (2001). Crustal stress field in southern California and its implication for fault mechanics. *Journal of Geophysical Research*, 106(B10), 21,859–21,882. <https://doi.org/10.1029/2001JB000292>
- Hofmann-Wellenhof, B., Lichtenegger, H., & Collins, J. (1992). *Global Positioning System theory and practice*. Vienna, New York: Springer-Verlag. <https://doi.org/10.1007/978-3-7091-5126-6>
- Holzer, T. L. (1979). Elastic expansion of the lithosphere caused by groundwater depletion. *Journal of Geophysical Research*, 84(B9), 4689–4698. <https://doi.org/10.1029/JB084iB09p04689>
- Howell, S., Smith-Konter, B., Frazer, N., Tong, X., & Sandwell, D. (2016). The vertical fingerprint of earthquake cycle loading in southern California. *Nature Geoscience*, 9(8), 611–614. <https://doi.org/10.1038/ngeo2741>
- Huang, W.-J., Johnson, K. M., Fukuda, J., & Yu, S.-B. (2010). Insights into active tectonics of eastern Taiwan from analyses of geodetic and geologic data. *Journal of Geophysical Research*, 115, B03413. <https://doi.org/10.1029/2008JB006208>
- Hubbard, J., Shaw, J. H., Dolan, J., Pratt, T. L., McAuliffe, L., & Rockwell, T. K. (2014). Structure and seismic hazard of the Ventura Avenue anticline and Ventura Fault, California: Prospect for large, multisegment ruptures in the western Transverse Ranges. *Bulletin of the Seismological Society of America*, 104(3), 1070–1087. <https://doi.org/10.1785/0120130125>
- Jackson, J., & Molnar, P. (1990). Active faulting and block rotations in the western Transverse Ranges, California. *Journal of Geophysical Research*, 95(B13), 22,073–22,087. <https://doi.org/10.1029/JB095iB13p22073>
- Johnson, K., Hammond, W. C., & Burgette, R. (2014). Geodetic constraints on shortening, uplift, and fault slip across the Ventura Basin, SCEC Annual meeting, Palm Springs, CA, Sept. 6–10, 2014.
- Kohler, M. D., & Davis, P. M. (1997). Crustal thickness variations in southern California from Los Angeles region seismic experiment passive phase teleseismic travel times. *Bulletin of the Seismological Society of America*, 87(5), 1330–1344.
- Kreemer, C., Hammond, W. C., Blewitt, G., Holland, A., & Bennett, R. A. (2012). A geodetic strain rate model for the southwestern United States, (scale 1:1,500,000), Nevada Bureau of Mines and Geology publication M178.
- Lanari, R., Lundgren, P., Manzo, M., & Casu, F. (2004). Satellite radar interferometry time series analysis of surface deformation for Los Angeles, California. *Geophysical Research Letters*, 31, L23613. <https://doi.org/10.1029/2004GL021294>
- Luyendyk, B. P., Kamerling, M. J., Terres, R. R., & Hornafius, J. S. (1985). Simple shear of southern California during Neogene time suggested by paleomagnetic declinations. *Journal of Geophysical Research*, 90(B14), 12,454–12,466. <https://doi.org/10.1029/JB090iB14p12454>
- Marshall, S. T., Funning, G. J., Krueger, H. E., Owen, S. E., & Loveless, J. P. (2017). Mechanical models favor a ramp geometry for the Ventura-pitas point fault, California. *Geophysical Research Letters*, 44, 1311–1319. <https://doi.org/10.1002/2016GL072289>
- Marshall, S. T., Funning, G. J., & Owen, S. E. (2013). Fault slip rates and interseismic deformation in the western transverse ranges, California. *Journal of Geophysical Research: Solid Earth*, 118, 4511–4534. <https://doi.org/10.1002/jgrb.50312>
- Massonnet, D., & Feigl, K. L. (1998). Radar interferometry and its application to changes in the Earth's surface. *Reviews of Geophysics*, 36(4), 441–500. <https://doi.org/10.1029/97RG03139>
- McAuliffe, L. J., Dolan, J. F., Rhodes, E. J., Hubbard, J., Shaw, J. H., & Pratt, T. L. (2015). Paleoseismologic evidence for large-magnitude (mw 7.5–8.0) earthquakes on the Ventura blind thrust fault: Implications for multifault ruptures in the transverse ranges of southern California. *Geosphere*, 11(5), 1629–1650. <https://doi.org/10.1130/GES01123.1>
- McCaffrey, R. (2005). Block kinematics of the Pacific–North America plate boundary in the southwestern United States from inversion of GPS, seismological, and geologic data. *Journal of Geophysical Research*, 110, B07401. <https://doi.org/10.1029/2004JB003307>
- McCrory, P., & Lajoie, K. R. (1979). Marine terrace deformation, San Diego county, California. *Tectonophysics*, 52(1–4), 407–408. [https://doi.org/10.1016/0040-1951\(79\)90254-3](https://doi.org/10.1016/0040-1951(79)90254-3)
- Meade, B. J., & Hager, B. H. (2005). Block models of crustal motion in southern California constrained by GPS measurements. *Journal of Geophysical Research*, 110, B03403. <https://doi.org/10.1029/2004JB003209>
- Nicholson, C., Kamerling, M. J., Sorlien, C. C., Hopps, T. E., & Gratier, J.-P. (2007). Subsidence, compaction and gravity-sliding: Implications for active 3D geometry, dynamic rupture, and seismic hazard of active basin-bounding faults in southern California. *Bulletin of the Seismological Society of America*, 97(5), 1607–1620. <https://doi.org/10.1785/0120060236>
- Niemi, N. A., Oskin, M., & Rockwell, T. K. (2008). Southern California earthquake center geologic vertical motion database. *Geochemistry, Geophysics, Geosystems*, 9, Q07010. <https://doi.org/10.1029/2008GC002017>
- Pinter, N., Sorlien, C. C., & Scott, A. T. (2003). Fault-related fold growth and isostatic subsidence, California Channel islands. *American Journal of Science*, 303(4), 300–318. <https://doi.org/10.2475/ajs.303.4.300>
- Rockwell, T. K., Clark, K., Gamble, L., Oskin, M. E., Haaker, E. C., & Kennedy, G. L. (2016). Large transverse range earthquakes cause coastal upheaval near Ventura, Southern California. *Bulletin of the Seismological Society of America*, 106(6), 2706–2720. <https://doi.org/10.1785/0120150378>

- Rockwell, T. K., Keller, E. A., & Dembroff, G. R. (1988). Quaternary rate of folding of the Ventura Avenue anticline, western Transverse Ranges, southern California. *GSA Bulletin*, 100(6), 850–858. [https://doi.org/10.1130/0016-7606\(1988\)100%3C0850:QROFOT%3E2.3.CO;2](https://doi.org/10.1130/0016-7606(1988)100%3C0850:QROFOT%3E2.3.CO;2)
- Sandwell, D., Zeng, Y., Shen, Z.-K., Crowell, B., Murray, J., McCaffrey, R., & Xu, X. (2016). The SCEC community geodetic model V1: Horizontal velocity grid, SCEC contribution #6967, Presentation at 2016 SCEC Annual Meeting.
- Savage, J. C. (1983). A dislocation model of strain accumulation and release at a subduction zone. *Journal of Geophysical Research*, 88(B6), 4984–4996. <https://doi.org/10.1029/JB088iB06p04984>
- Scherneck, H.-G. (1991). A parametrized solid earth tide model and ocean tide loading effects for global geodetic baseline measurements. *Geophysical Journal International*, 106(3), 677–694. <https://doi.org/10.1111/j.1365-246X.1991.tb06339.x>
- Sen, P. K. (1968). Estimates of the regression coefficient based on Kendall's tau. *Journal of the American Statistical Association*, 63(324), 1379–1389. <https://doi.org/10.1080/01621459.1968.10480934>
- Shen, Z.-K., Jackson, D. D., & Ge, B. X. (1996). Crustal deformation across and beyond the Los Angeles basin from geodetic measurements. *Journal of Geophysical Research*, 101(B12), 27,957–27,980. <https://doi.org/10.1029/96JB02544>
- Shirazaee, M. (2015). A seamless multitrack multitemporal InSAR algorithm. *Geochemistry, Geophysics, Geosystems*, 16, 1656–1669. <https://doi.org/10.1002/2015GC005759>
- Sneed, M., Brandt, J., & Solt, M. (2013). Land subsidence along the Delta-Mendota Canal in the northern part of the San Joaquin Valley, California, 2003–10. U.S. Geol. Surv. Sci. Invest. Rep. 2013–5142, 87 p. <https://doi.org/10.3133/sir20135142>
- Sorlien, C. C., Seeber, L., Broderick, K. G., Luyendyk, B. P., Fisher, M. A., Sliter, R. W., & Normark, W. R. (2013). The Palos Verdes anticlinorium along the Los Angeles, California coast: Implications for underlying thrust faulting. *Geochemistry, Geophysics, Geosystems*, 14, 1866–1890. <https://doi.org/10.1002/ggge.20112>
- Spada, G., & Galassi, G. (2012). New estimates of secular sea level rise from tide gauge data and GIA modelling. *Geophysical Journal International*, 191, 1067–1094. <https://doi.org/10.1111/j.1365-246X.2012.05663.x>
- Stammer, D., Cazenave, A., Ponte, R. M., & Tamisiea, M. E. (2013). Causes for contemporary regional sea level changes. *Annual Review of Marine Science*, 5(1), 21–46. <https://doi.org/10.1146/annurev-marine-121211-172406>
- Stein, R. S., Whalen, C. T., Holdahl, S. R., Strange, W. E., & Thatcher, W. (1986). Saugus-Palmdale, California, field test for refraction error in historical leveling surveys. *Journal of Geophysical Research*, 91(B9), 9031–9044. <https://doi.org/10.1029/JB091iB09p09031>
- Strange, W. (1981). The impact of refraction correction on leveling interpretations in Southern California. *Journal of Geophysical Research*, 86(B4), 2809–2824. <https://doi.org/10.1029/JB086iB04p02809>
- Tape, C., Musé, P., Simons, M., Dong, D., & Webb, F. (2009). Multiscale estimation of GPS velocity fields. *Geophysical Journal International*, 179(2), 945–971. <https://doi.org/10.1111/j.1365-246X.2009.04337.x>
- Theil, H. (1950). A rank-invariant method of linear and polynomial regression analysis. *Indagationes Mathematicae*, 12, 85–91.
- Tong, X., Sandwell, D. T., & Smith-Konter, B. (2013). High-resolution interseismic velocity data along the San Andreas fault from GPS and InSAR. *Journal of Geophysical Research: Solid Earth*, 118, 369–389. <https://doi.org/10.1029/2012JB009442>
- Tregoning, P., & Watson, C. (2009). Atmospheric effects and spurious signals in GPS analyses. *Journal of Geophysical Research*, 114, B09403. <https://doi.org/10.1029/2009JB006344>
- United States Geological Survey and California Geological Survey (2006). Quaternary fault and fold database for the United States. Retrieved from <https://earthquake.usgs.gov/hazards/qfaults/>
- United States Geological Survey California Water Science Center (2017). Map downloaded February 2017. Retrieved from https://ca.water.usgs.gov/land_subsidence/california-subsidence-areas.html
- van Dam, T. M., Blewitt, G., & Heflin, J. B. (1994). Atmospheric pressure loading effects on Global Positioning System coordinate determinations. *Journal of Geophysical Research*, 99(B12), 23,939–23,950. <https://doi.org/10.1029/94JB02122>
- Wahr, J., Khan, S. A., van Dam, T., Liu, L., van Angelen, J. H., van den Broeke, M. R., & Meertens, C. M. (2013). The use of GPS horizontals for loading studies, with applications to northern California and southeast Greenland. *Journal of Geophysical Research: Solid Earth*, 118, 1795–1806. <https://doi.org/10.1002/jgrb.50104>
- Watson, K. M., Bock, Y., & Sandwell, D. T. (2002). Satellite interferometric observations of displacements associated with seasonal ground-water in the Los Angeles basin. *Journal of Geophysical Research*, 107(B4), 2074. <https://doi.org/10.1029/2001JB000470>
- Wdowinski, S., Bock, Y., Zhang, J., Feng, P., & Genrich, J. (1997). Southern California permanent GPS geodetic array: Spatial filtering of daily positions for estimating coseismic and postseismic displacements induced by the 1992 Landers earthquake. *Journal of Geophysical Research*, 102(B8), 18,057–18,070. <https://doi.org/10.1029/97JB01378>
- Wei, M., Sandwell, D., & Smith-Konter, B. (2010). Optimal combination of InSAR and GPS for measuring interseismic crustal deformation. *Journal Advances in Space Research*, 46(2), 236–249. <https://doi.org/10.1016/j.asr.2010.03.013>
- Werner, C., Wegmüller, U., Strozzi, T., & Wiesmann, A. (2000). Gamma SAR and interferometric processing software, ERS - ENVISAT symposium, Gothenburg, Sweden, 16–20 Oct. 2000.
- Williams, S. D. P. (2008). CATS: GPS coordinate time series analysis software. *GPS Solutions*, 12(2), 147–153. <https://doi.org/10.1007/s10291-007-0086-4>
- Wisely, B. A., & Schmidt, D. (2010). Deciphering vertical deformation and poroelastic parameters in a tectonically active fault-bound aquifer using InSAR and well level data, San Bernardino basin, California. *Geophysical Journal International*, 181, 1185–1200.
- Wöppelmann, G., & Marcos, M. (2016). Vertical land motion as a key to understanding sea level change and variability. *Reviews of Geophysics*, 54, 64–92. <https://doi.org/10.1002/2015RG000502>
- Yang, W., & Hauksson, E. (2013). The tectonic crustal stress field and style of faulting along the Pacific North America plate boundary in Southern California. *Geophysical Journal International*, 194(1), 100–117. <https://doi.org/10.1093/gji/ggt113>
- Yerkes, R. F., & Lee, W. H. K. (1979). Late Quaternary deformation in the western Transverse Ranges, California, in earthquake activity and Quaternary deformation of the western Transverse Ranges, California, Geological Survey Circular 799-B.
- Yerkes, R. F., & Lee, W. H. K. (1987). Late Quaternary deformation in the western Transverse Ranges. *Chapter 4 in Recent Reverse Faulting in the Transverse Ranges. U.S. Geological Survey Professional Paper* (Vol. 1339, pp. 71–133). Washington, DC: United States Government Printing Office.
- Yerkes, R. F., Sarna-Wojcicki, A. M., & Lajoie, K. R. (1987). Geology and Quaternary deformation of the Ventura area. *Chapter 11 in Recent Reverse Faulting in the Transverse Ranges, U.S. Geological Survey Professional Paper* (Vol. 1339, pp. 169–178). Washington, DC: United States Government Printing Office.
- Zumberge, J. F., Heflin, M. B., Jefferson, D. C., Watkins, M. M., & Webb, F. H. (1997). Precise point positioning for the efficient and robust analysis of GPS data from large networks. *Journal of Geophysical Research*, 102(B3), 5005–5017. <https://doi.org/10.1029/96JB03860>